2014 Spring

“Advanced Physical Metallurgy”

- Bulk Metallic Glasses -

05.29.2014

Eun Soo Park

Office: 33-313
Telephone: 880-7221
Email: espark@snu.ac.kr
Office hours: by appointment

Annealing of Bulk Metallic Glasses: SR → SCLR (& PS) → Crystallization

(a) Positive heat of mixing relation among constituent elements

- **Alloy design considering heat of mixing relation among constituent elements**

$\Delta H_{mix} \gg 0$ between A & B

⬇

creates (meta)stable miscibility gap in limited composition range

⬇

Phase separation to A-rich & B-rich phase

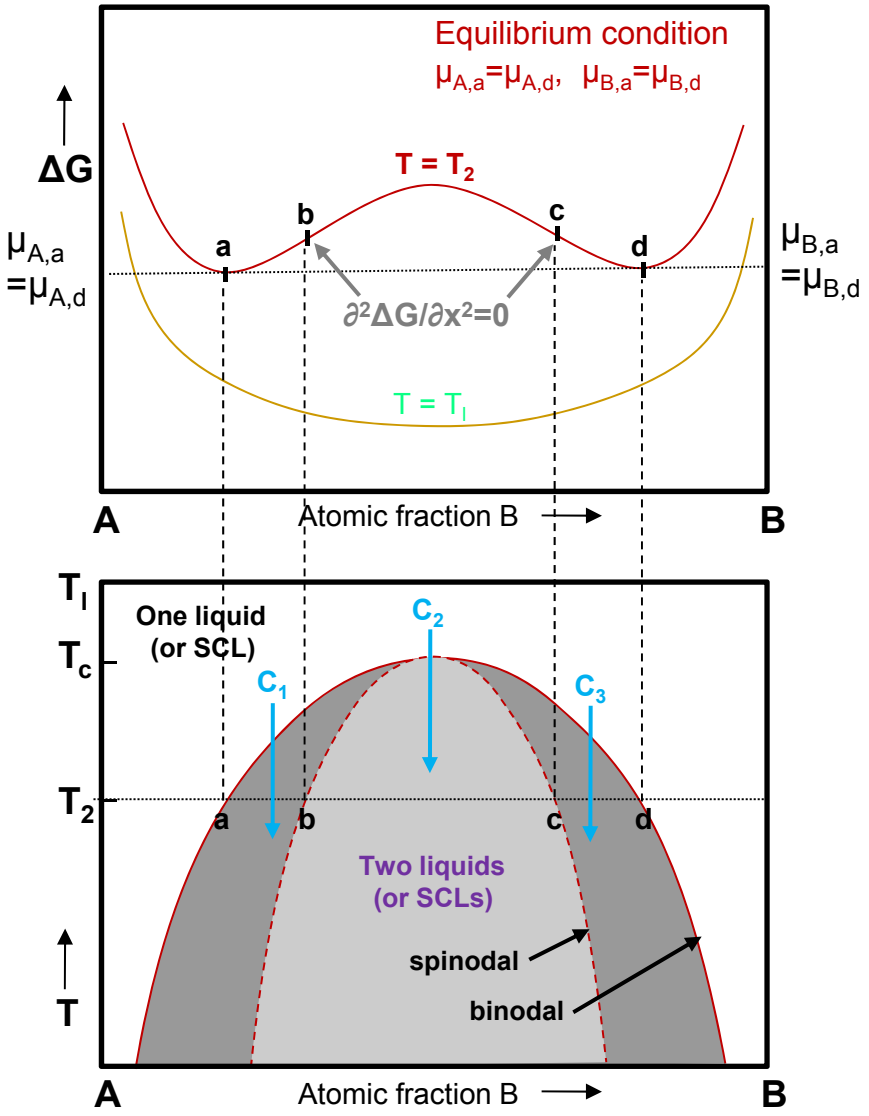

- **Different two-phase structure by initial composition before phase separation**

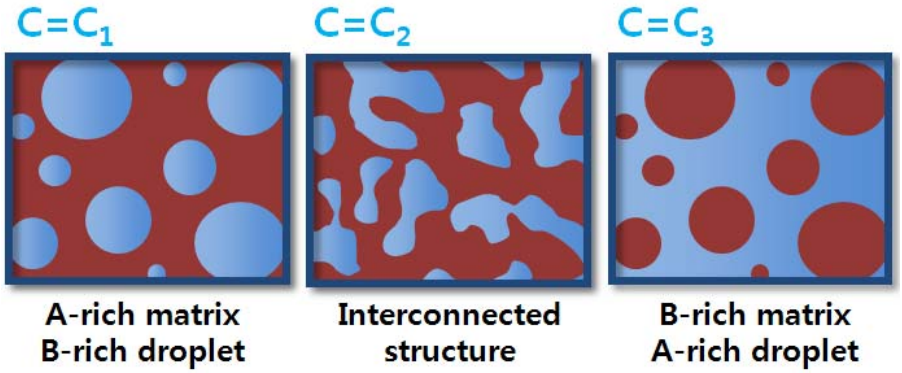

Nucleation and growth ↔ Spinodal decomposition without any barrier to the nucleation process

b. Phase separation in liquid state

* La-Zr-Al-Cu-Ni system

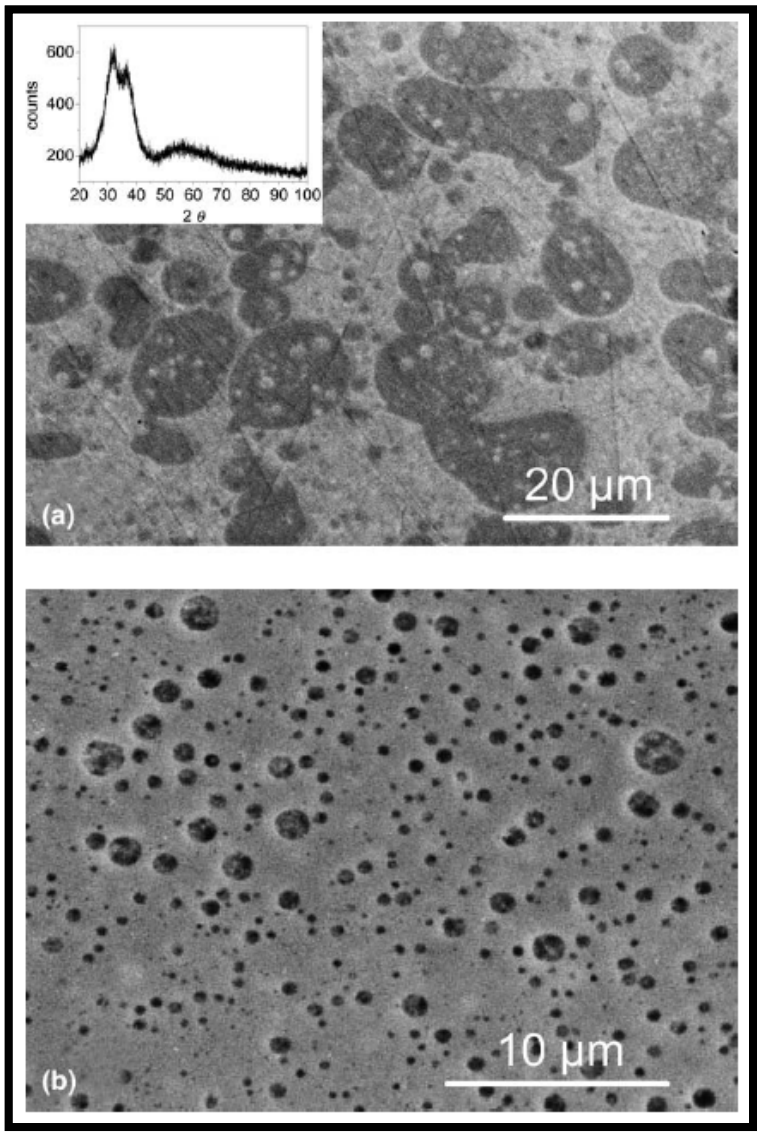

Kundig et al., *Acta Mat.*, 52 (2004) 2441-2448.

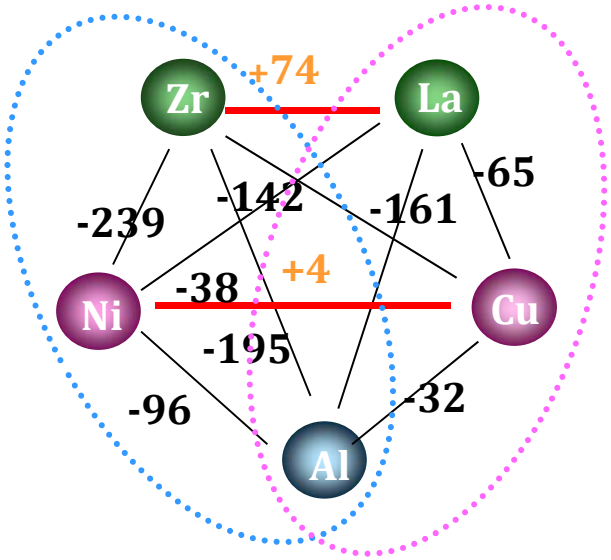

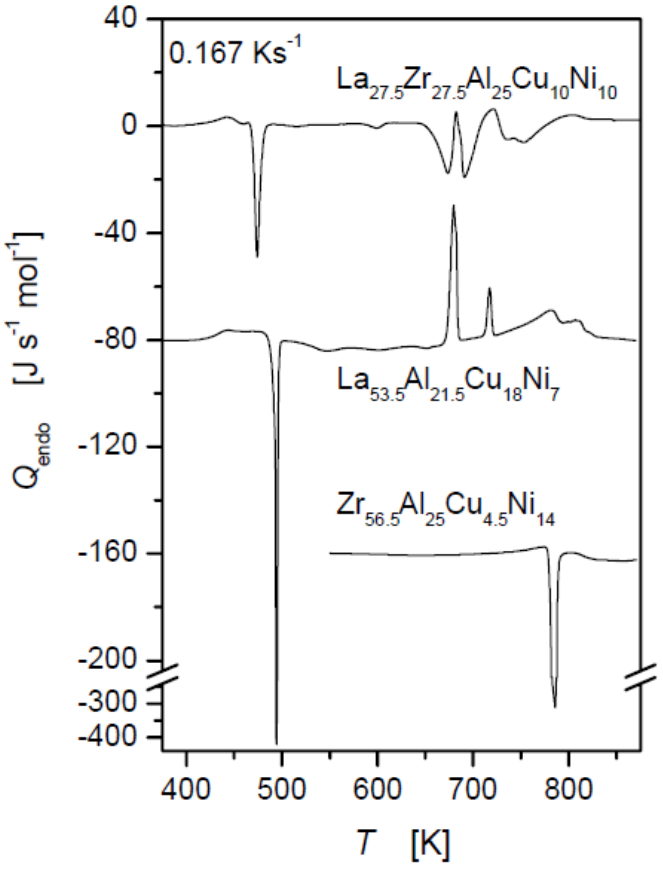

* La-Zr-Al-Cu-Ni system

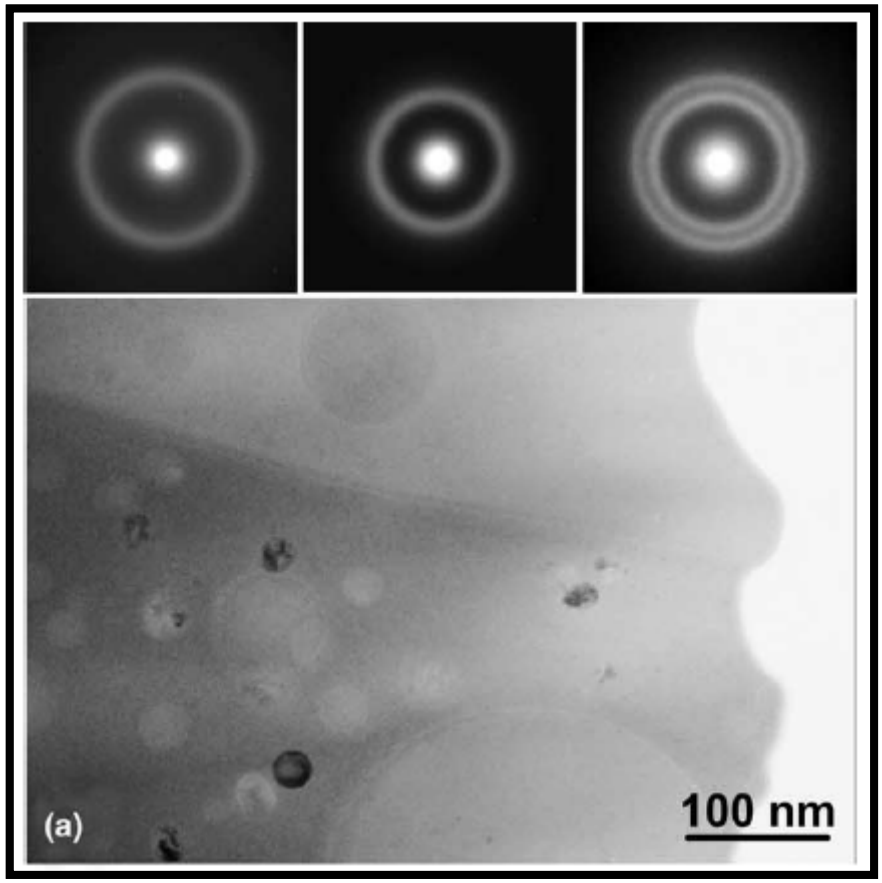

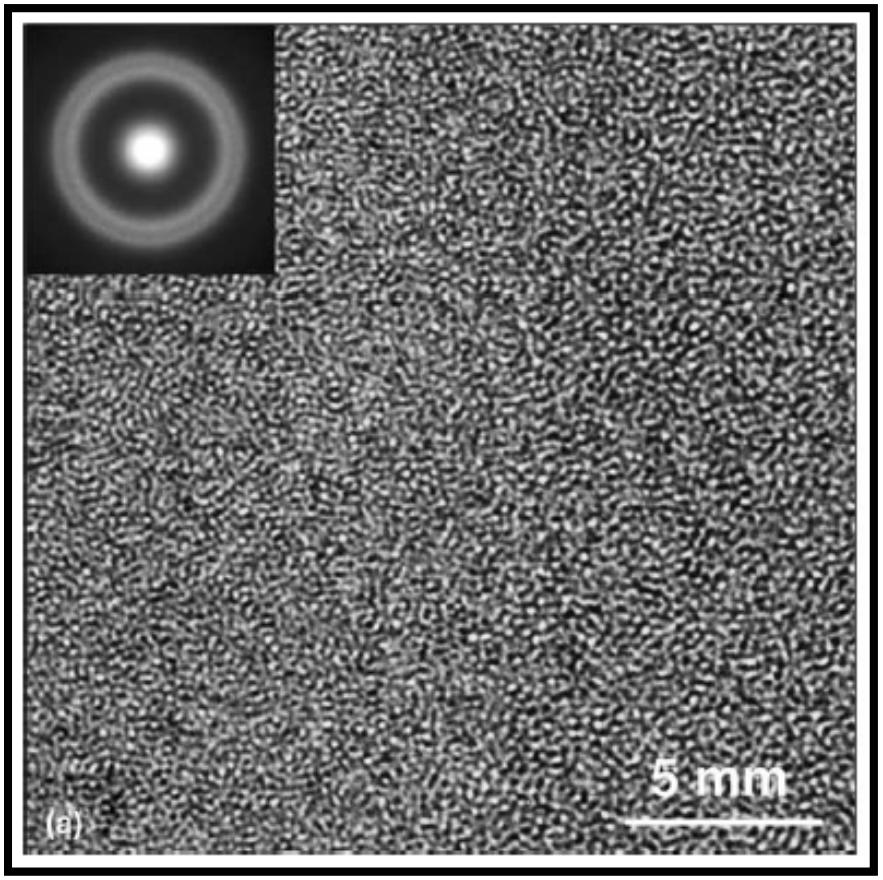

Kundig et al., *Acta Mat.*, 52 (2004) 2441-2448.

* La-Zr-Al-Cu-Ni system

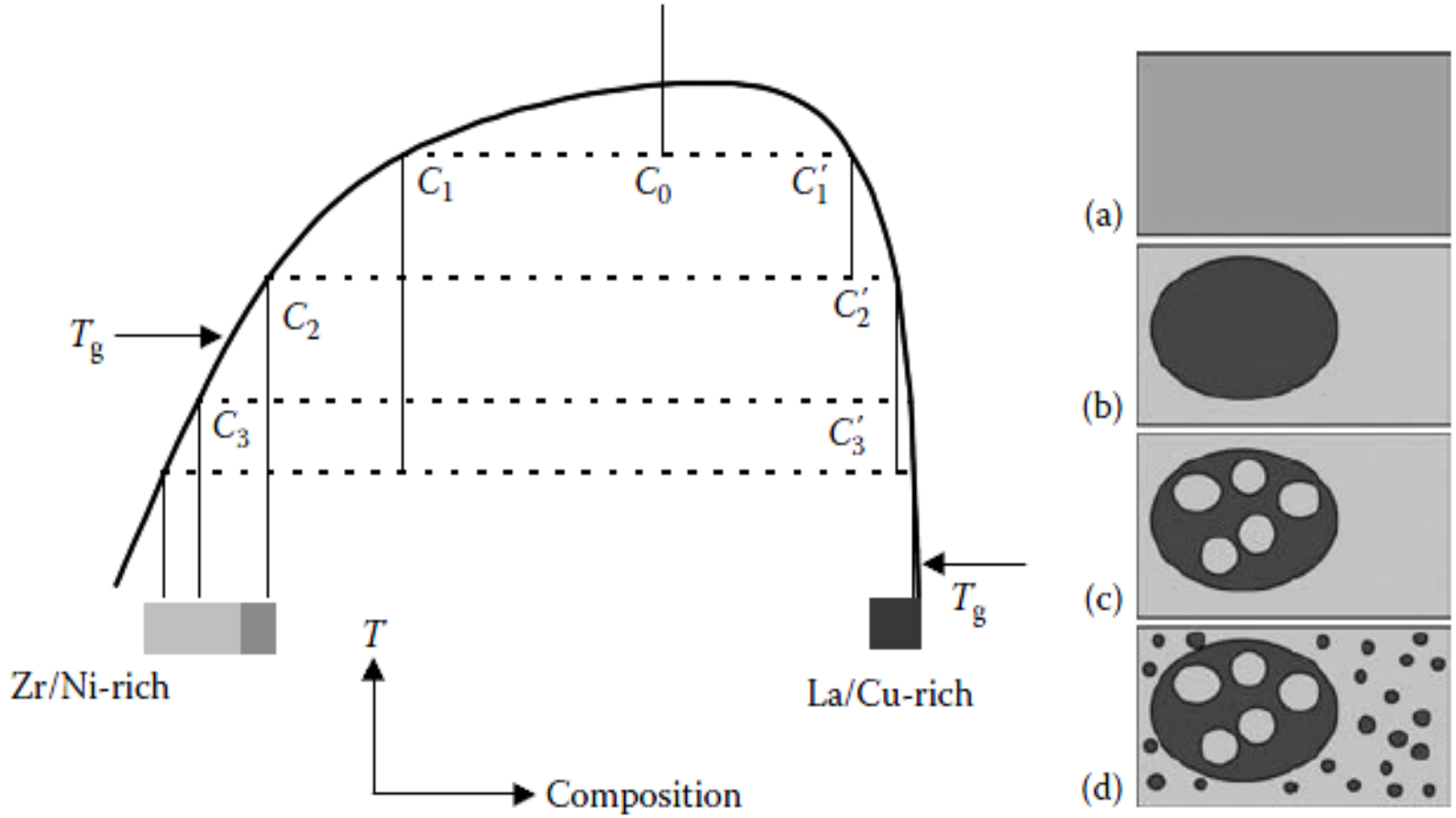

FIGURE 5.17
Schematic of the miscibility gap and the sequence of phase formation during cooling in the La–Zr–Al–Cu–Ni system. The positions of letters (a) to (d) in the diagram on the left correspond to the schematic microstructures (a) to (d) on the right. (Reprinted from Kündig, A.A. et al., *Acta Mater.*, 52, 2441, 2004. With permission.)

Shell/Yard region in phase separated structure

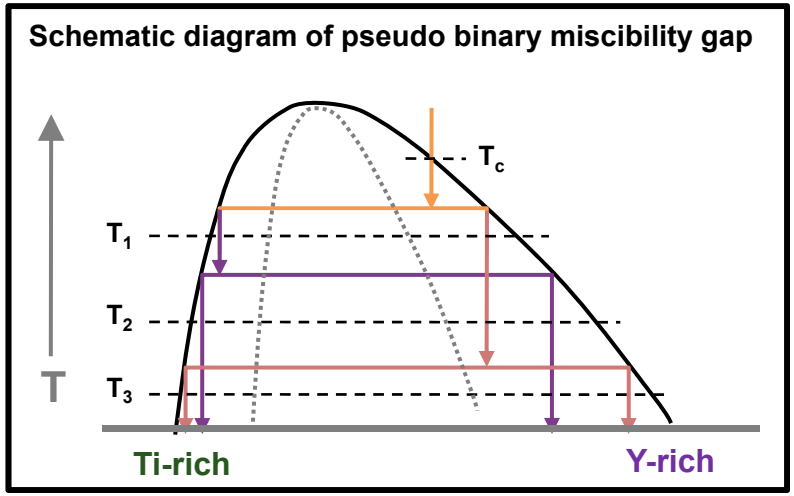

- Yard : Secondary phase-free region

  Shell : The layer enveloping primary phase by wetting

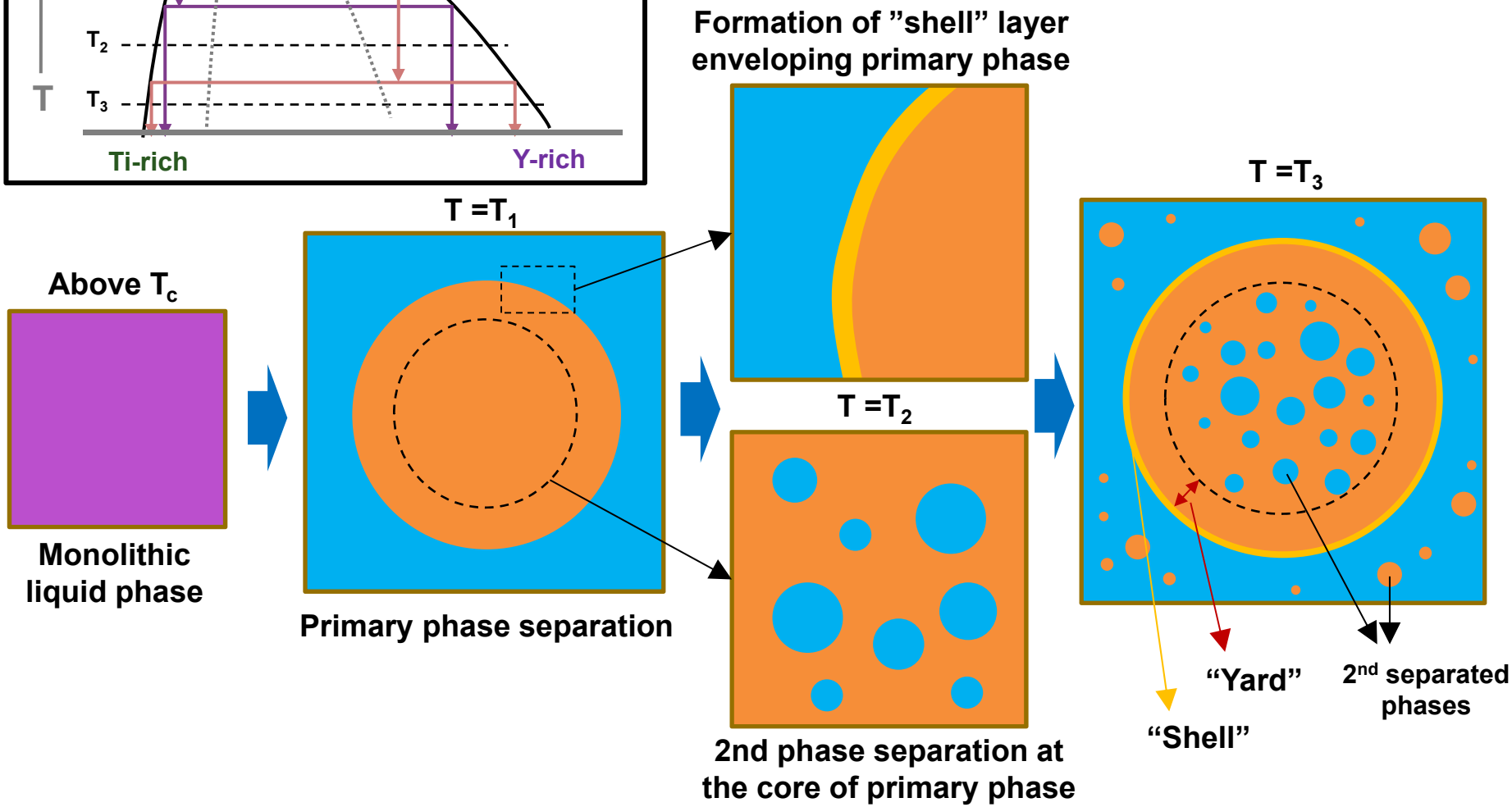

* Ti-Y-Al-Co system → $Ti_{24}Y_{18}La_{18}Al_{22}Co_{18}$ three different glassy phase

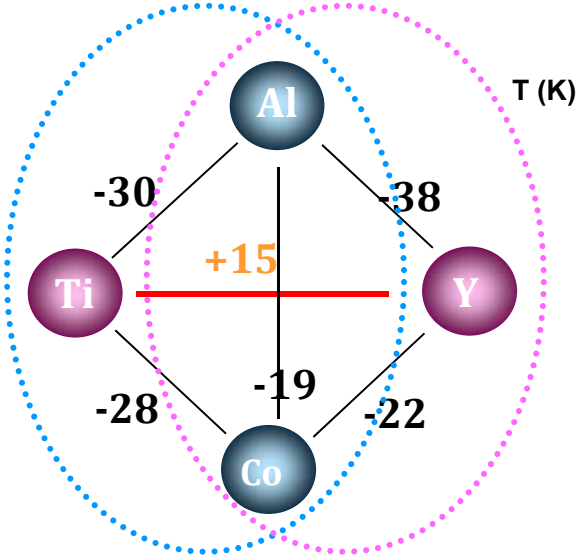

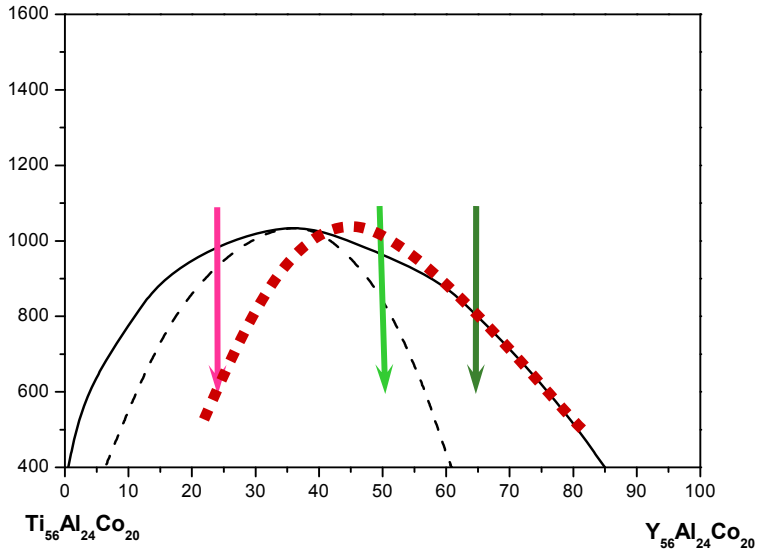

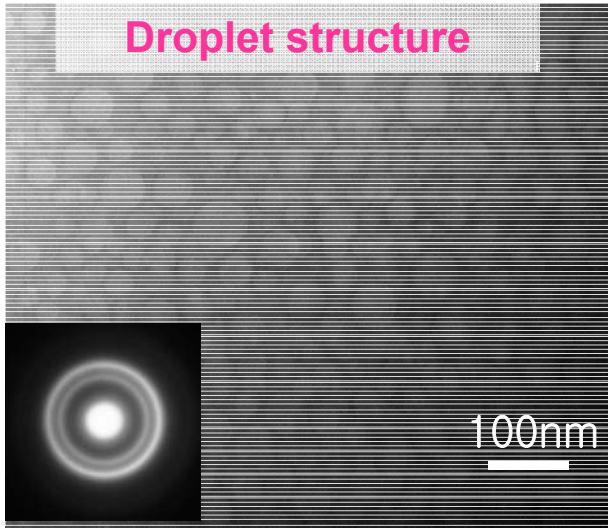

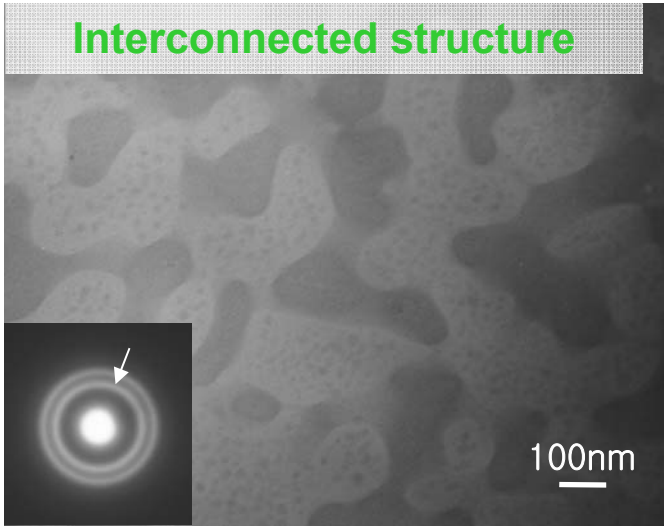

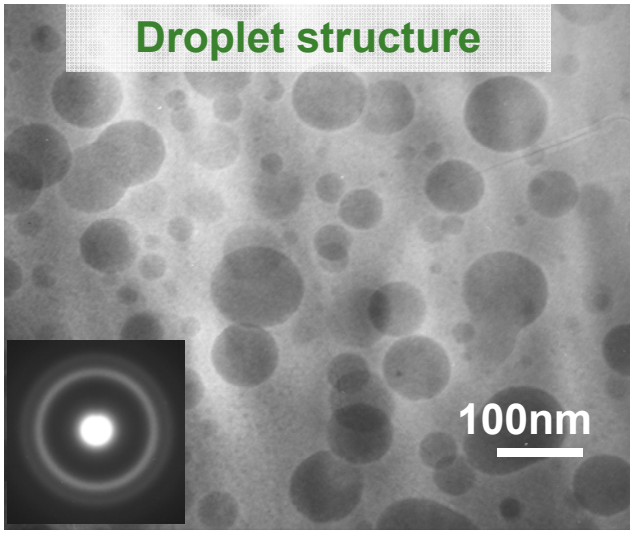

$(Y_{56}Al_{24}Co_{20})_{25}(Ti_{56}Al_{24}Co_{20})_{75}$ $(Y_{56}Al_{24}Co_{20})_{50}(Ti_{56}Al_{24}Co_{20})_{50}$ $(Y_{56}Al_{24}Co_{20})_{65}(Ti_{56}Al_{24}Co_{20})_{35}$

* Ni-Nb-Y system

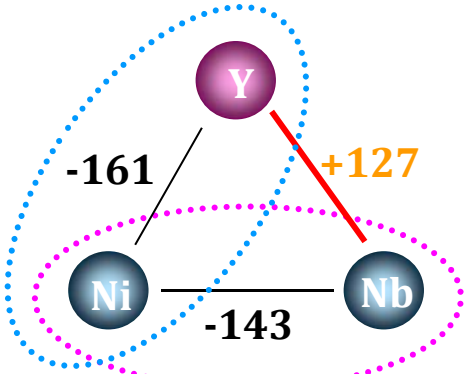

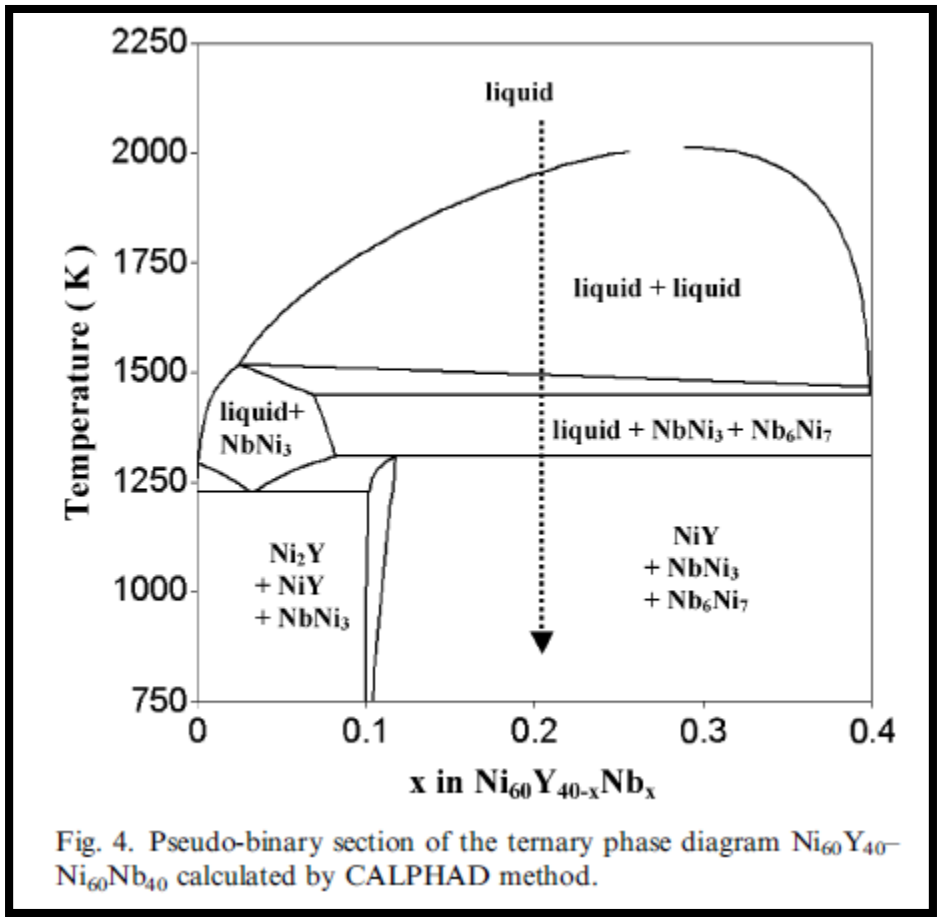

Fig. 4. Pseudo-binary section of the ternary phase diagram $Ni_{60}Y_{40}$–$Ni_{60}Nb_{40}$ calculated by CALPHAD method.

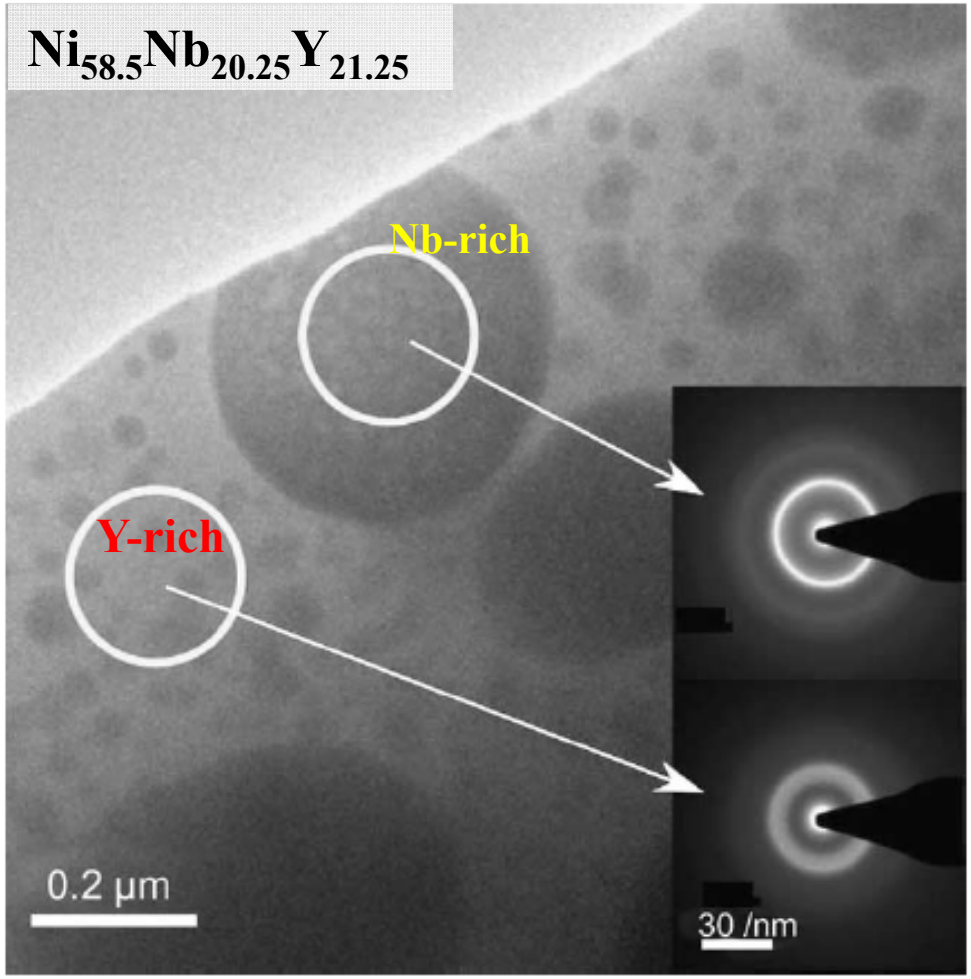

Mattern et al., *Scripta Mat.* 53 (2005) 271.
Mat. Sci. Eng. A, 449-451 (2007) 207.

Microstructure determining parameters of phase separation in metallic glasses

- ❖Composition
- ❖Glass-forming ability of the separated liquid
- ❖Critical temperature
- ❖Asymmetry of the spinodal curve / Decomposition range

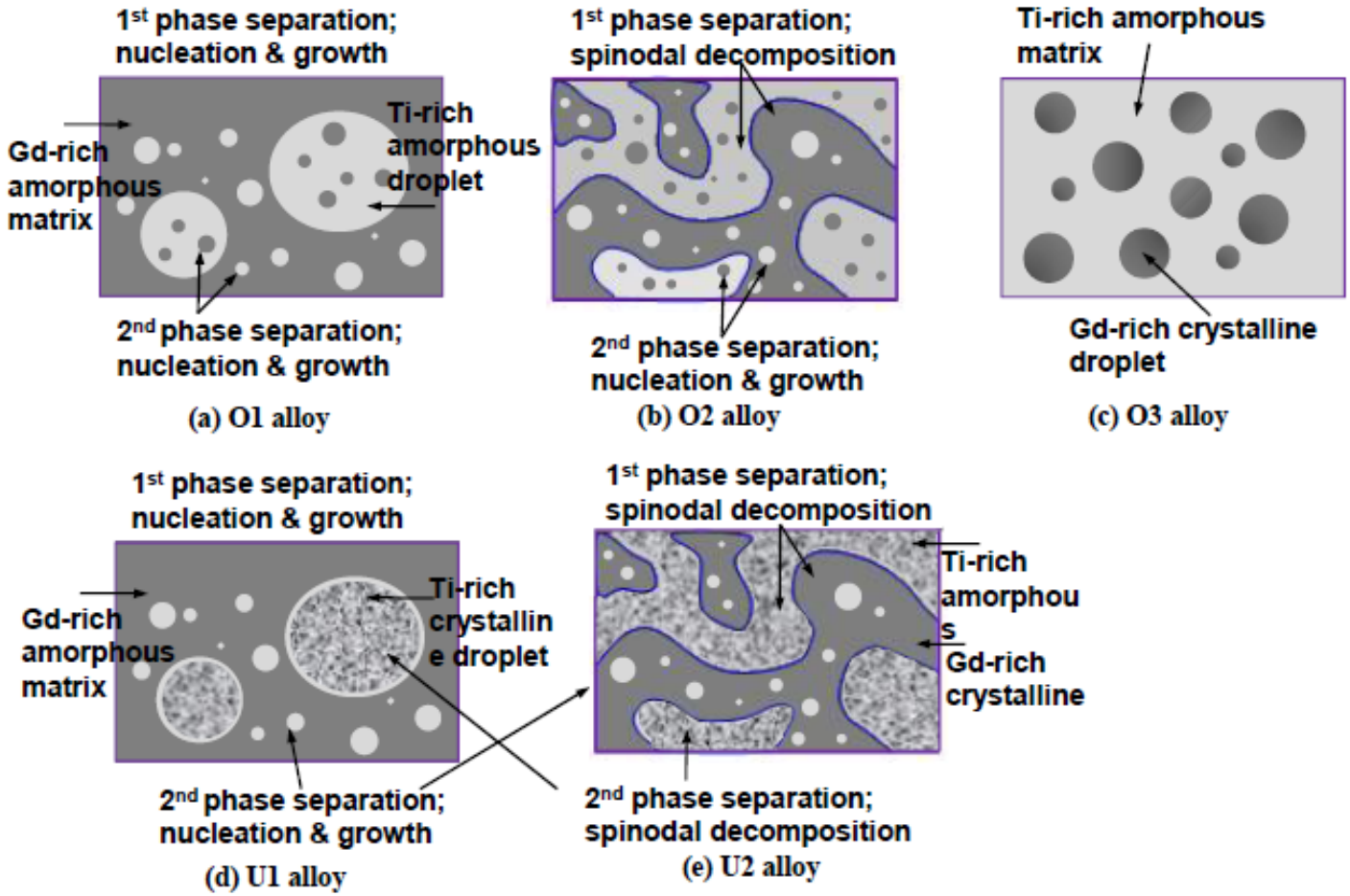

Thermodynamic calculation using CALPHAD

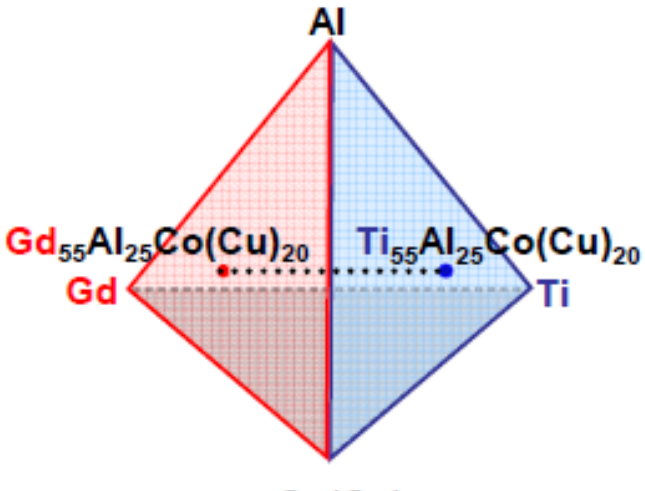

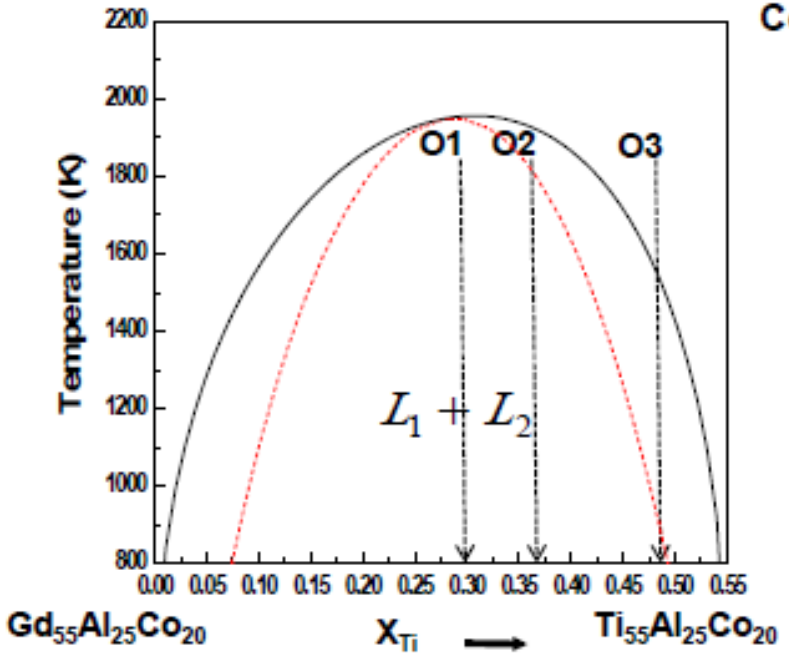

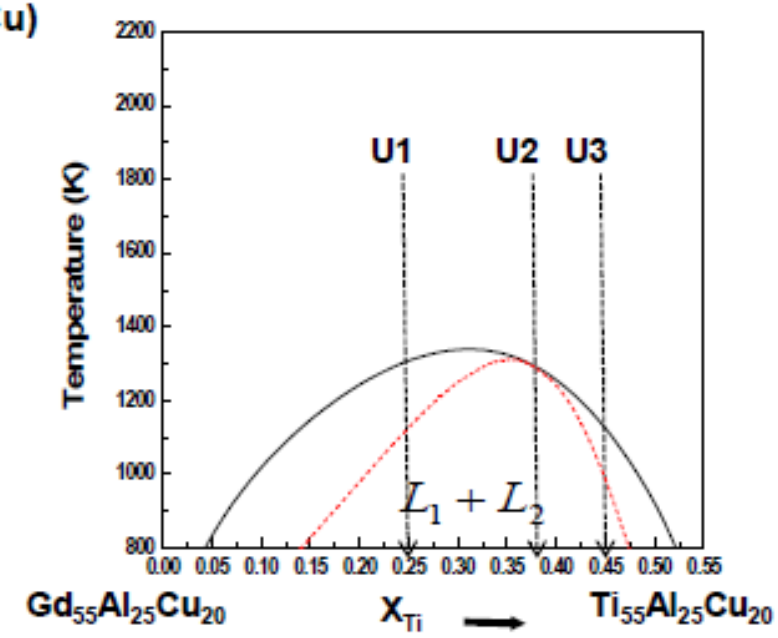

Microstructure evolution (GdTiAlCo)

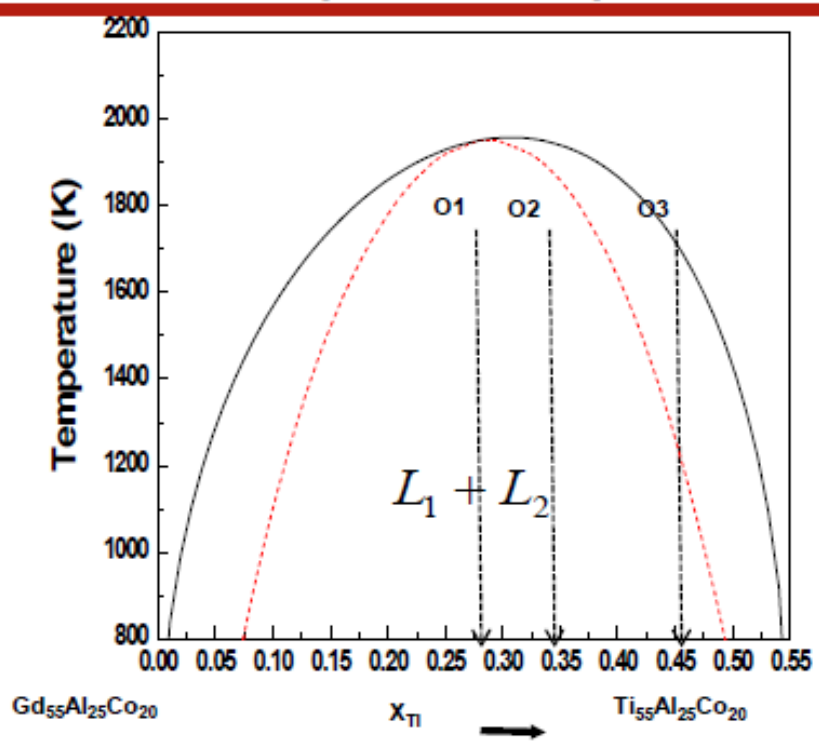

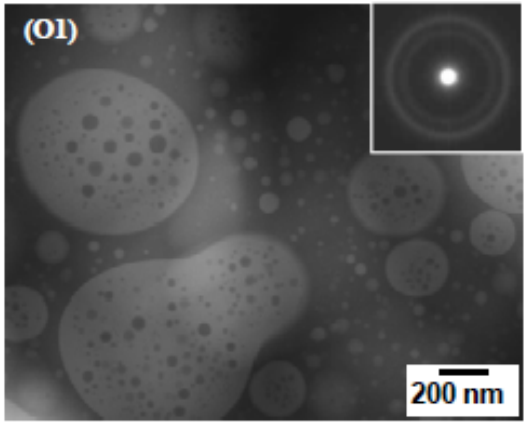

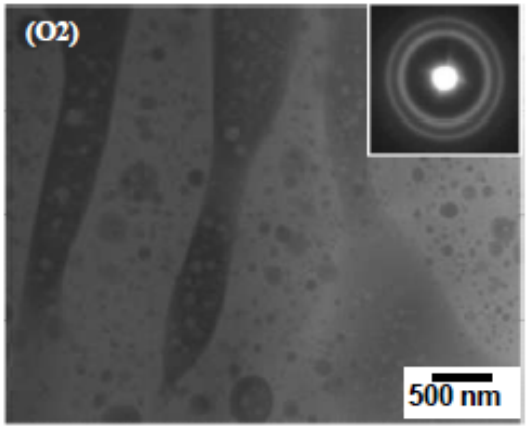

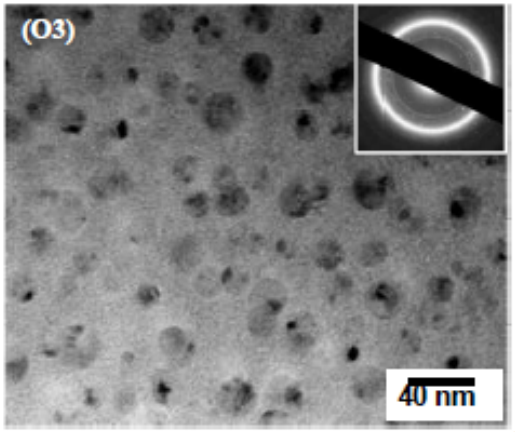

Chang et al., Acta Mater (2010)

Microstructure evolution (GdTiAlCu)

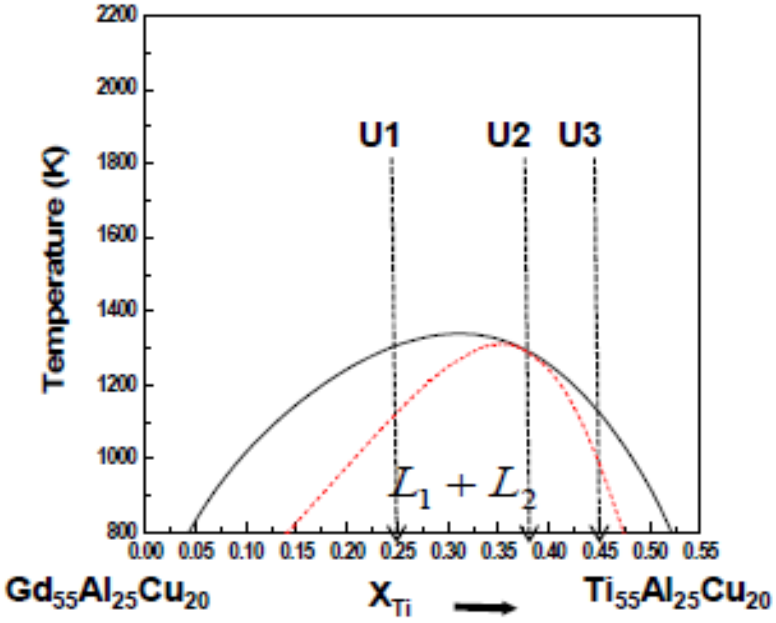

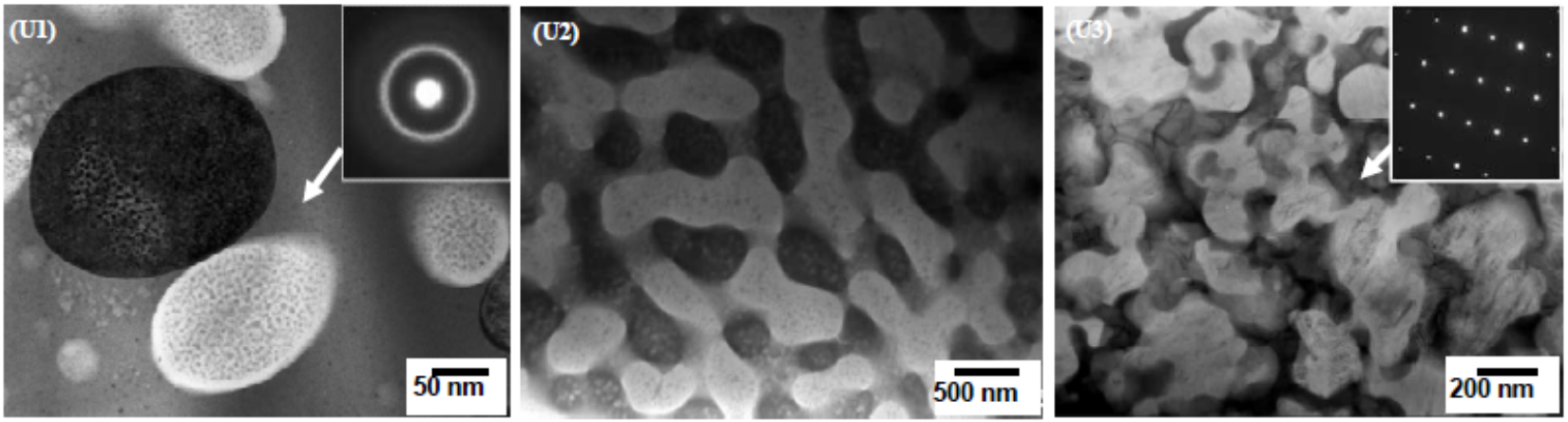

Chang et al., Acta Mater (2010)

Critical temperature

Spinodal critical point
$Gd_{25}Ti_{30}Al_{25}Co_{20}$ (at **1950 K**)

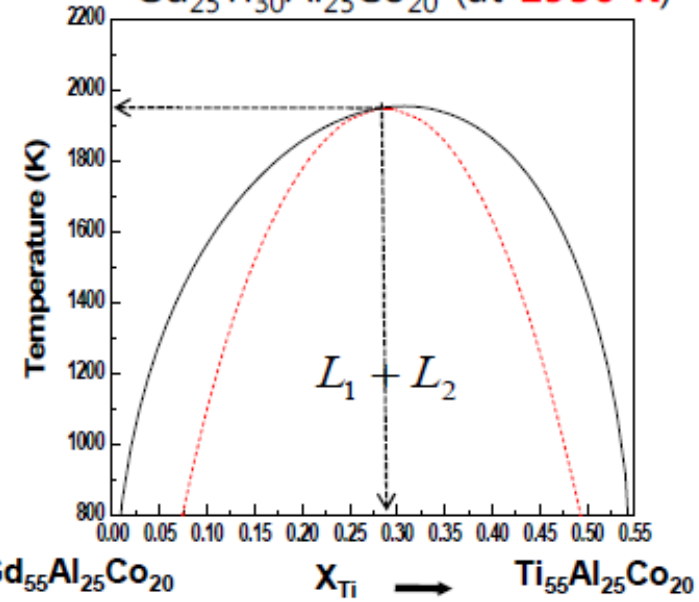

Spinodal critical point
$Gd_{18}Ti_{37}Al_{25}Cu_{20}$ (at **1300 K**)

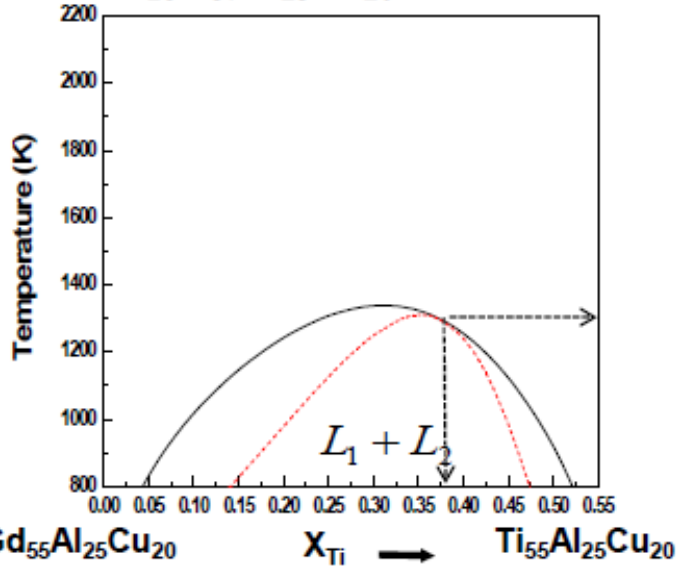

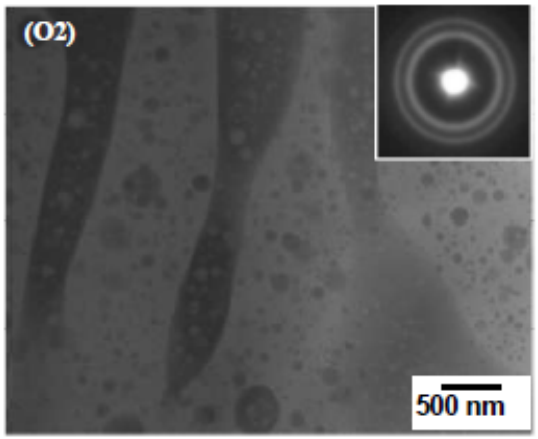

Scale of interconnected structure

←Several um

200~300 nm→

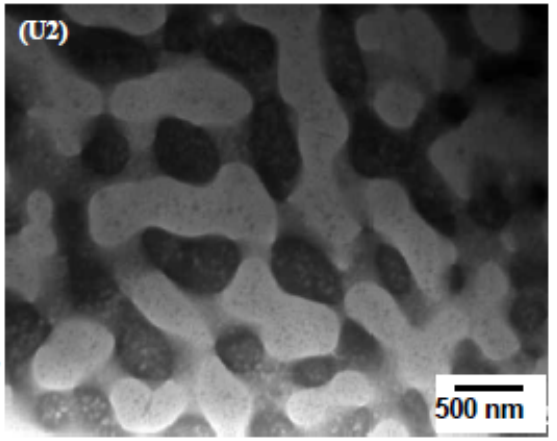

Asymmetry of spinodal curve / Decomposition range

❖ Symmetric spinodal curve / smaller decomposition range

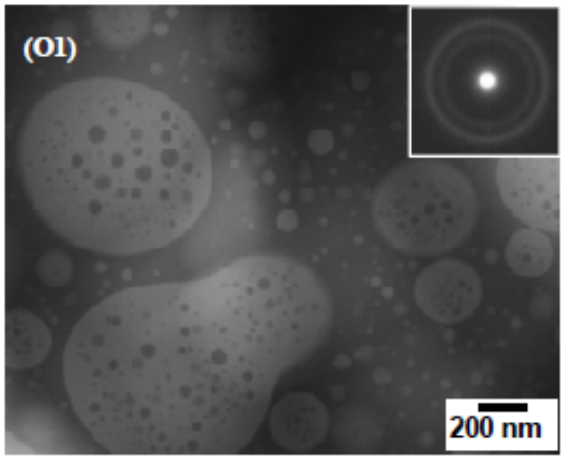

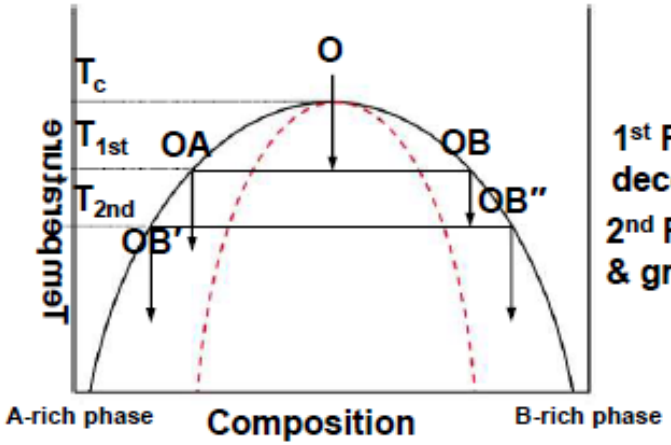

1st P.S.; spinodal decomposition

2nd P.S.; nucleation & growth

❖Asymmetric spinodal curve / larger decomposition range

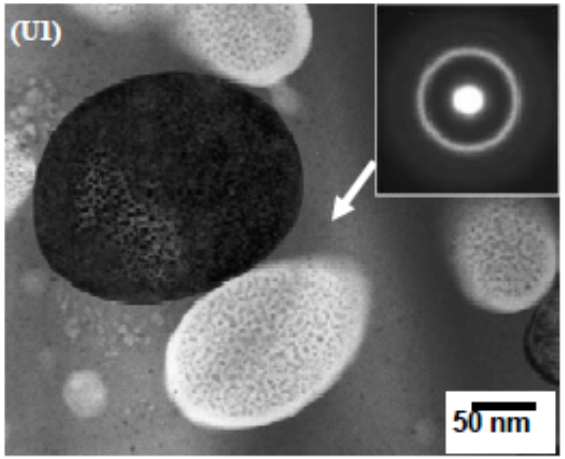

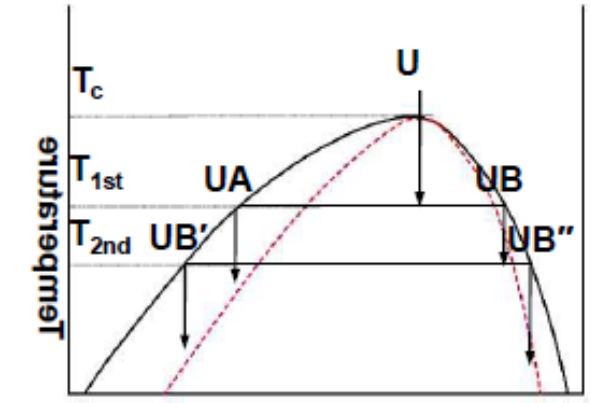

1st P.S.; spinodal decomposition

2nd P.S.; spinodal decomposition

(b) Significantly different heat of mixing relation among constituent elements

According to Meijering , a ternary alloy phase can decompose into two phases with different composition seven when the enthalpy of mixing is negative.

- Cu-Zr-Be ternary alloy system

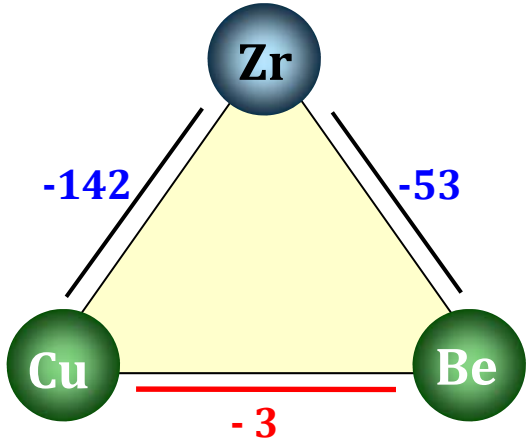

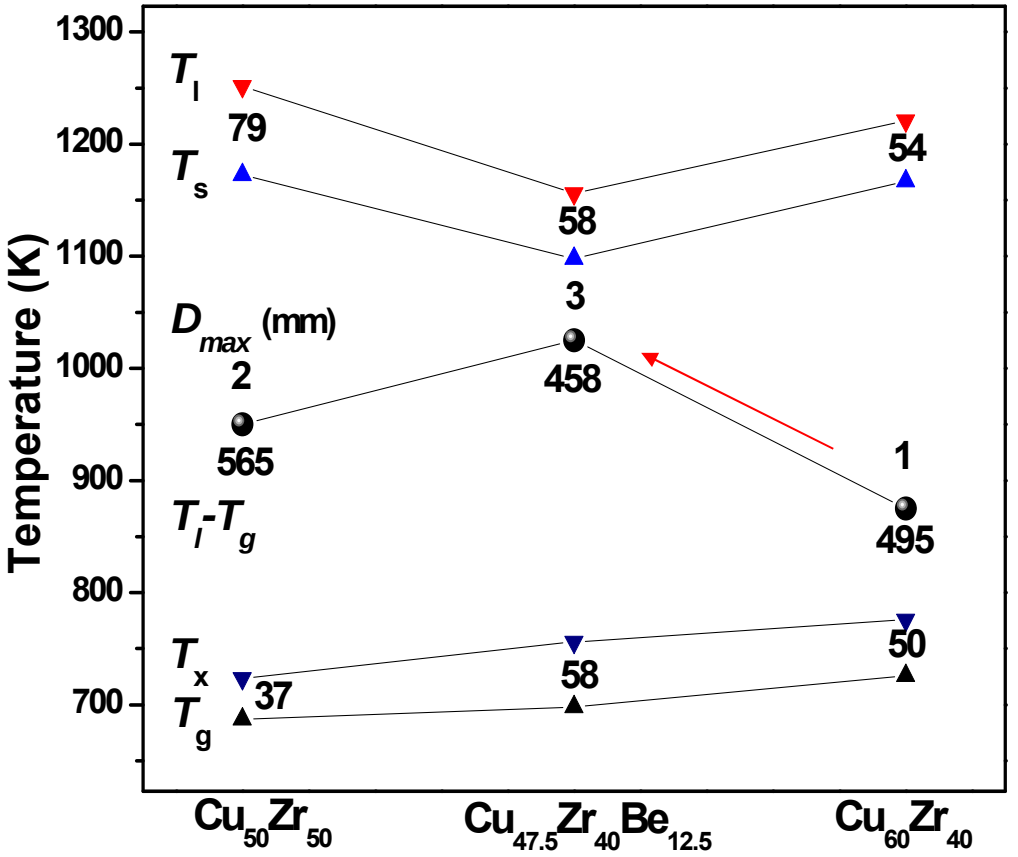

* ESPark, Acta Materialia (2008)

Cu-Zr-Be ternary alloy system: Cu-Zr & Zr-Be rich phases

- Compression test

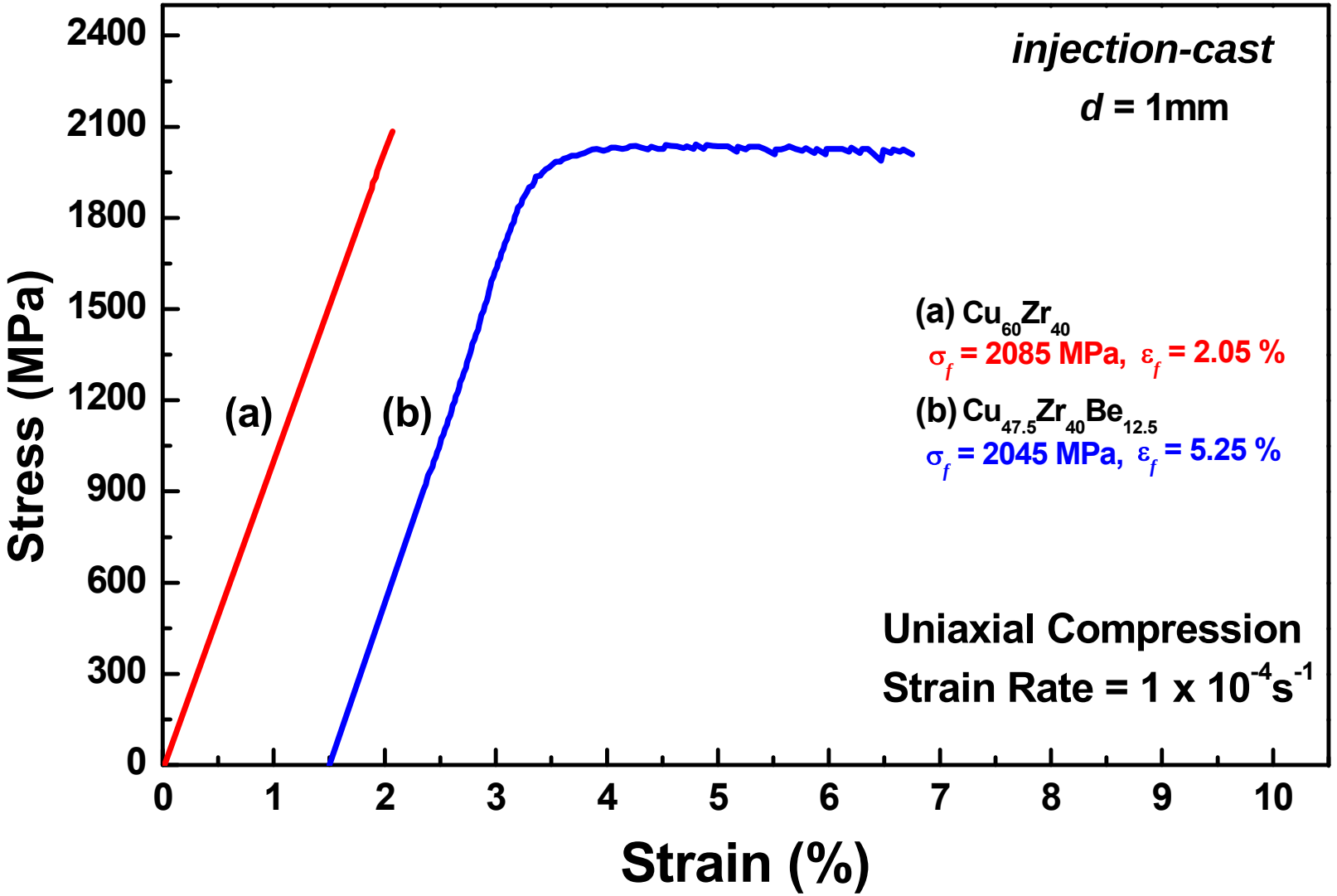

EXAFS analysis

	r (Å)		*N*		Total *N*	σ²	
	Cu-Cu	Cu-Zr	Cu-Cu	Cu-Zr		Cu-Cu	Cu-Zr
$Cu_{60}Zr_{40}$	2.49	2.69	3.0	3.7	6.7	0.0116	0.0233
$Cu_{47.5}Zr_{40}Be_{12.5}$	2.51	2.70	2.5	4.8	7.3	0.0107	0.0227
	Zr-Zr	Zr-Cu	Zr-Zr	Zr-Cu		Zr-Zr	Zr-Cu
$Cu_{60}Zr_{40}$	3.10	2.68	6.9	4.4	11.3	0.0263	0.0124
$Cu_{47.5}Zr_{40}Be_{12.5}$	3.12	2.69	6.2	3.5	9.7	0.0257	0.0130

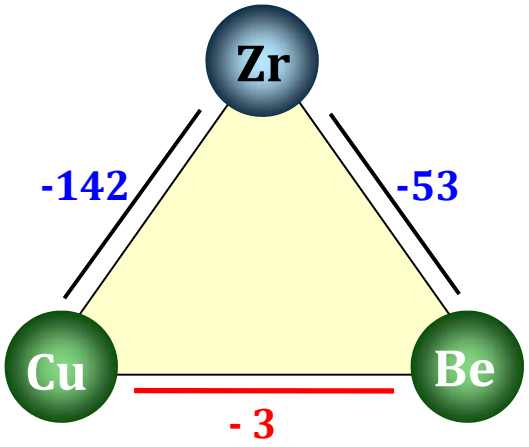

Atoimic diameter in Å: Cu-Cu = 2.56, Cu-Zr = 2.88, Zr-Zr = 3.20.

Cargill-Spaepen short-range order parameters, η

	Z_{AB}	<Z>	Z^*_{AB}	Z^{**}_{AB}	η
$Cu_{60}Zr_{40}$	3.7	8.540	3.416	3.546	0.043
$Cu_{47.5}Zr_{40}Be_{12.5}$	4.8	7.348	2.939	3.855	0.245

Cargill-Spaepen SRO parameter

$$\eta = Z_{AB} / Z^{**}_{AB} - 1$$

$$Z^{**}_{AB} = x_B Z_B Z_A / < Z >$$

η > 0

chemical ordering between AB nearest-neighbor pairs

Unique Composite Materials Using Miscibility Gap

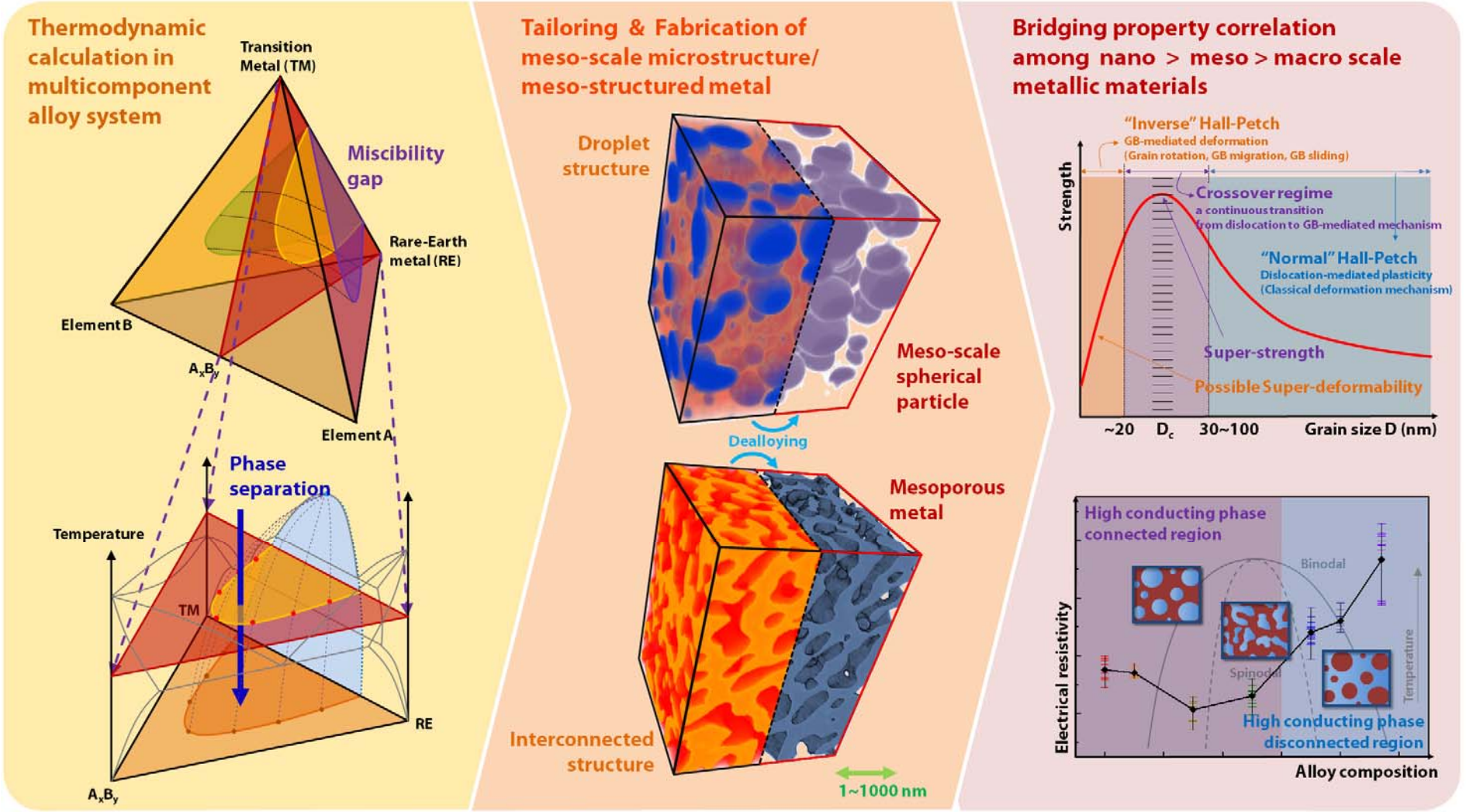

Phase separation by adding elements having PEM

* Substitution of Nd with Zr in Nd-Co-Al system

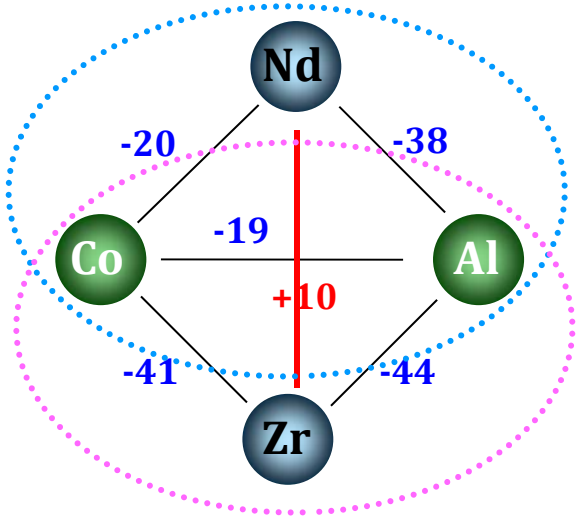

$Nd_{60}Al_{10}Co_{30}$ - 5mm

$Zr_{55}Al_{20}Co_{25}$ - 3mm

Possibility of two phase !!!

Nd-Co-Al, Zr-Co-Al

• Sripta Mater. 56, 197 (2007)

TEM results for $Nd_{30}Zr_{30}Al_{10}Co_{30}$ alloy

$Nd_{60}Al_{10}Co_{30}$
2.91 Å

$Nd_{30}Zr_{30}Al_{10}Co_{30}$
2.37 Å, 2.99 Å

$Zr_{60}Al_{10}Co_{30}$
2.40 Å

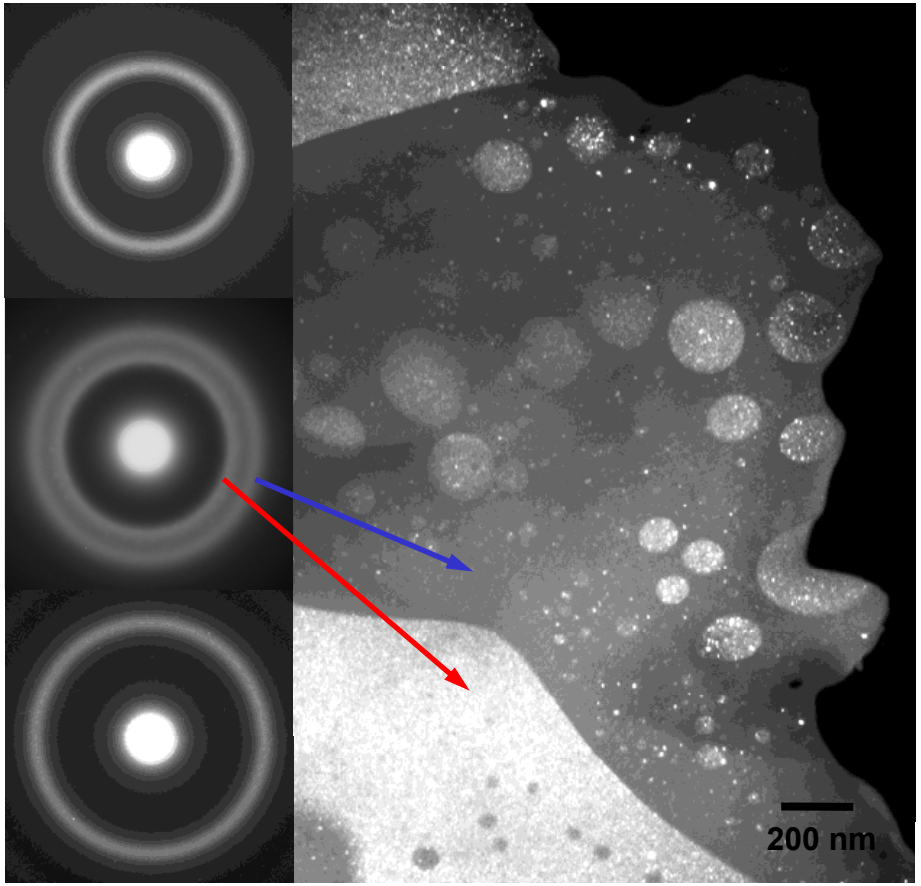

SADP and Dark-field TEM image

Measurement of viscosity using TMA

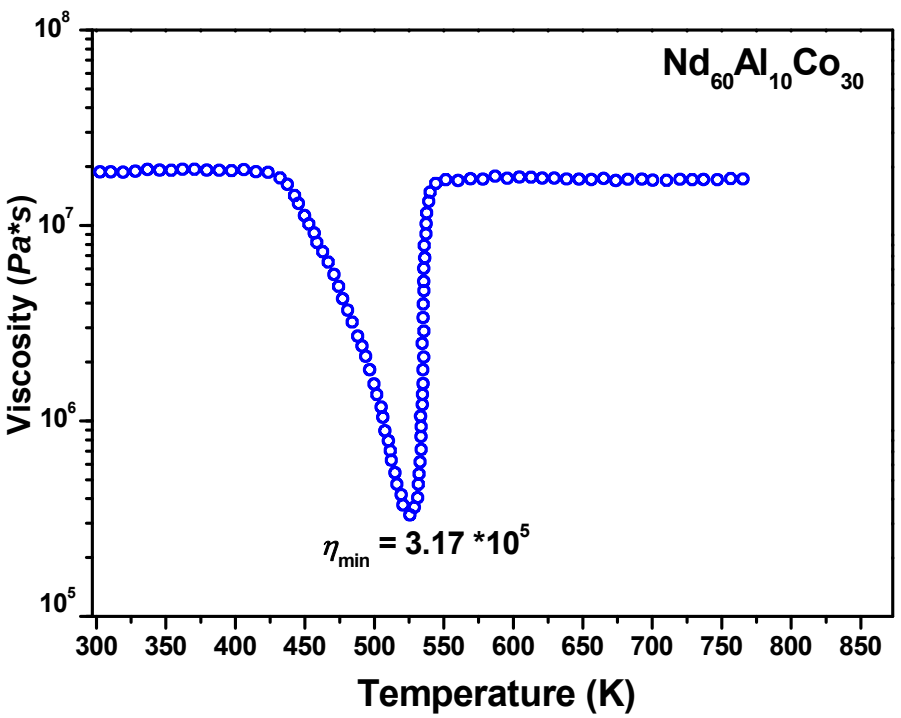

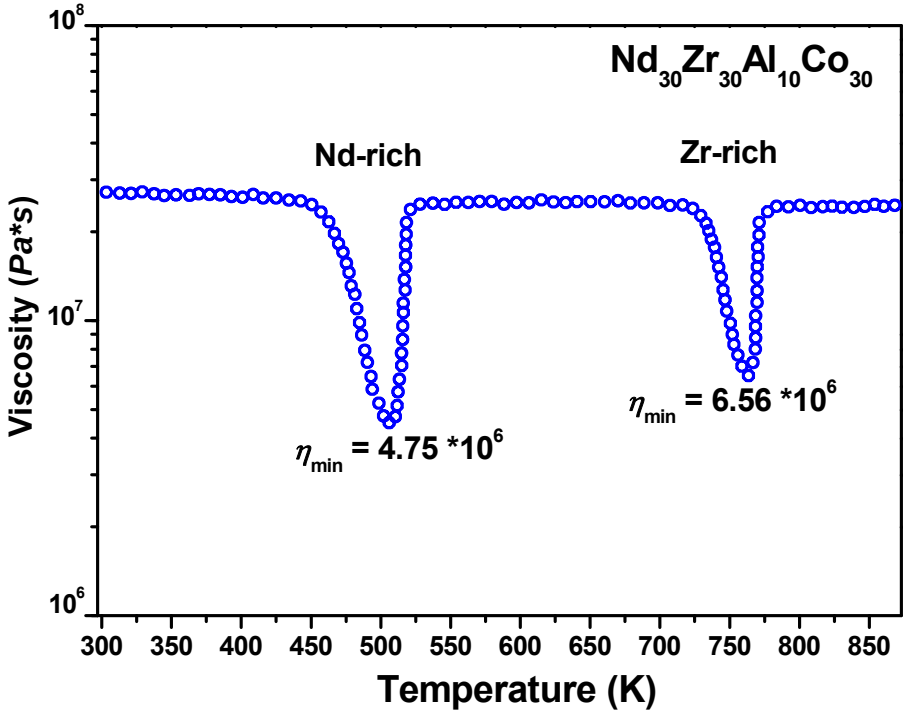

Selective partial devitrification (first SLR), followed by easy deformation of the amorphous/ crystalline composite structure (second SLR) is possible for this alloy system.

Measurement of magnetic property using VSM

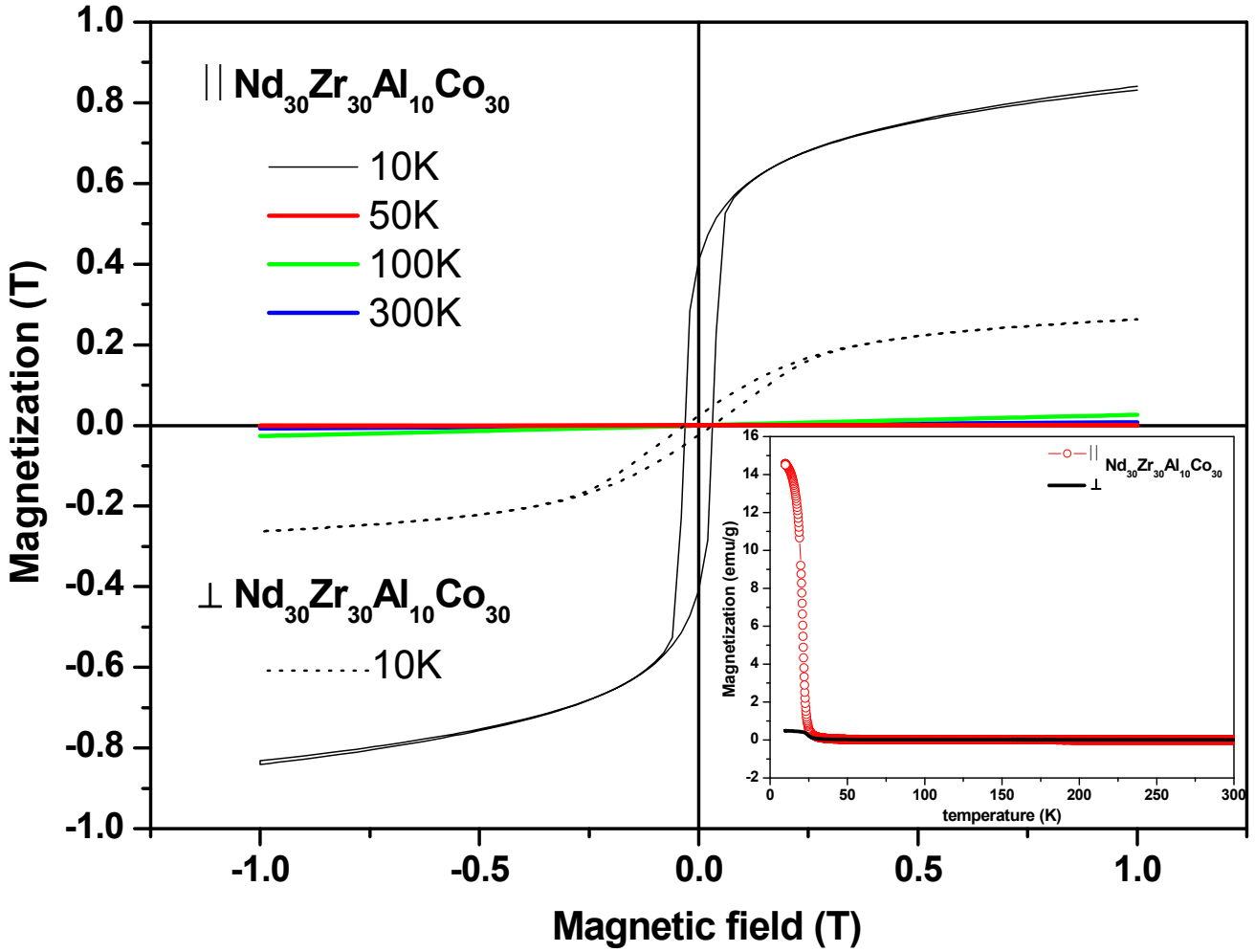

Directional changes of magnetic property in two-phase metallic glass

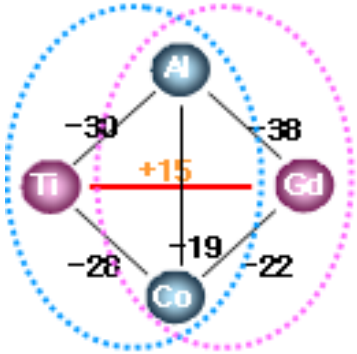

$Gd_{55}Al_{25}Co_{20}$

Ti

Zr

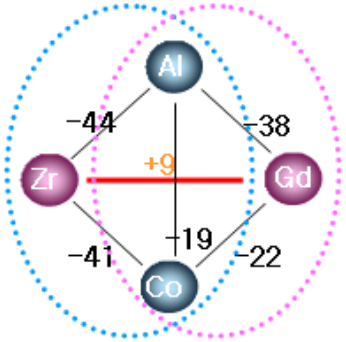

$Gd_{30}Ti_{25}Al_{25}Co_{20}$

$Gd_{30}Zr_{25}Al_{25}Co_{20}$

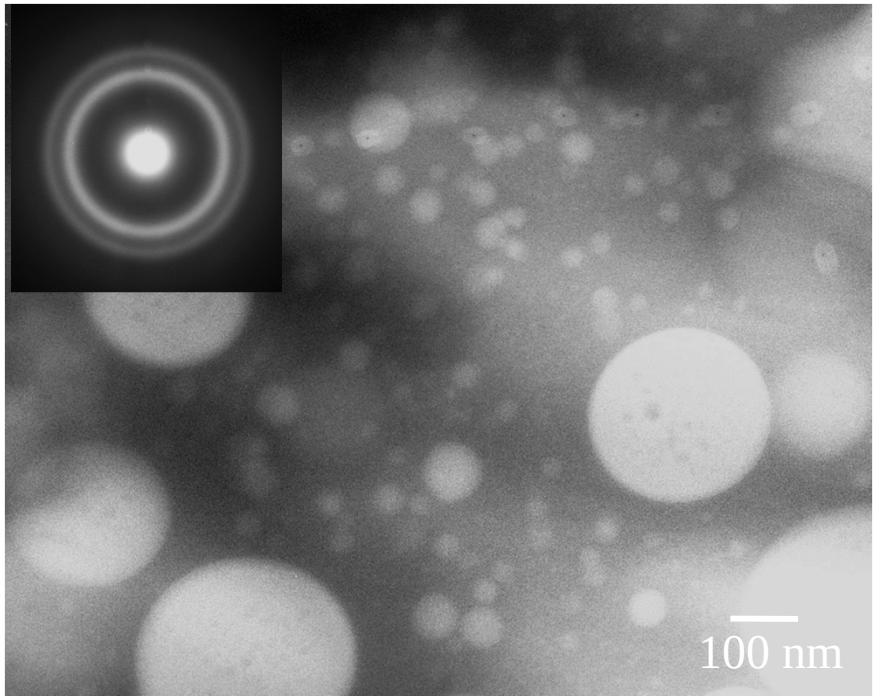

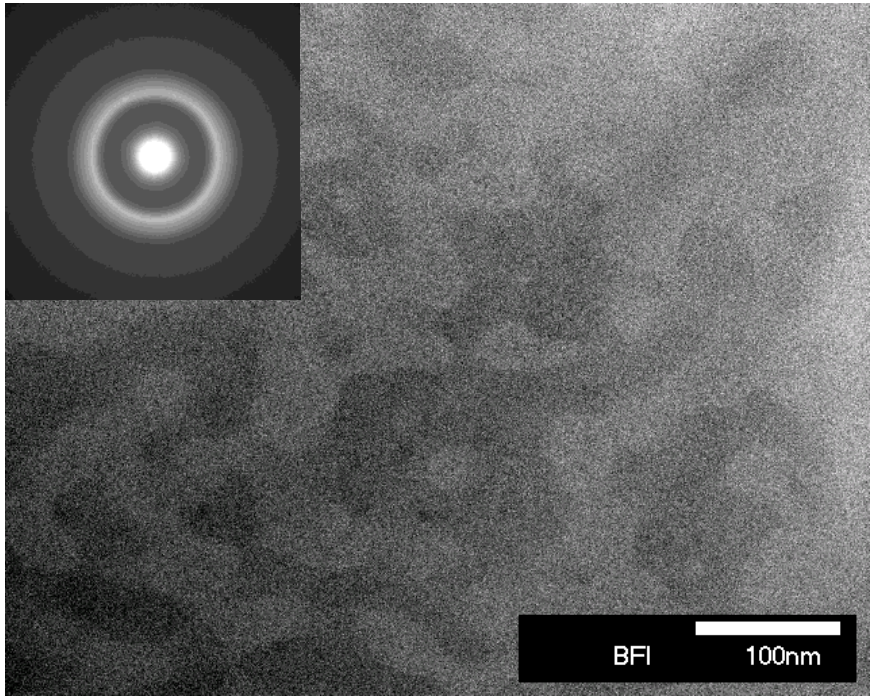

Droplet structure ⟷ Interconnected structure

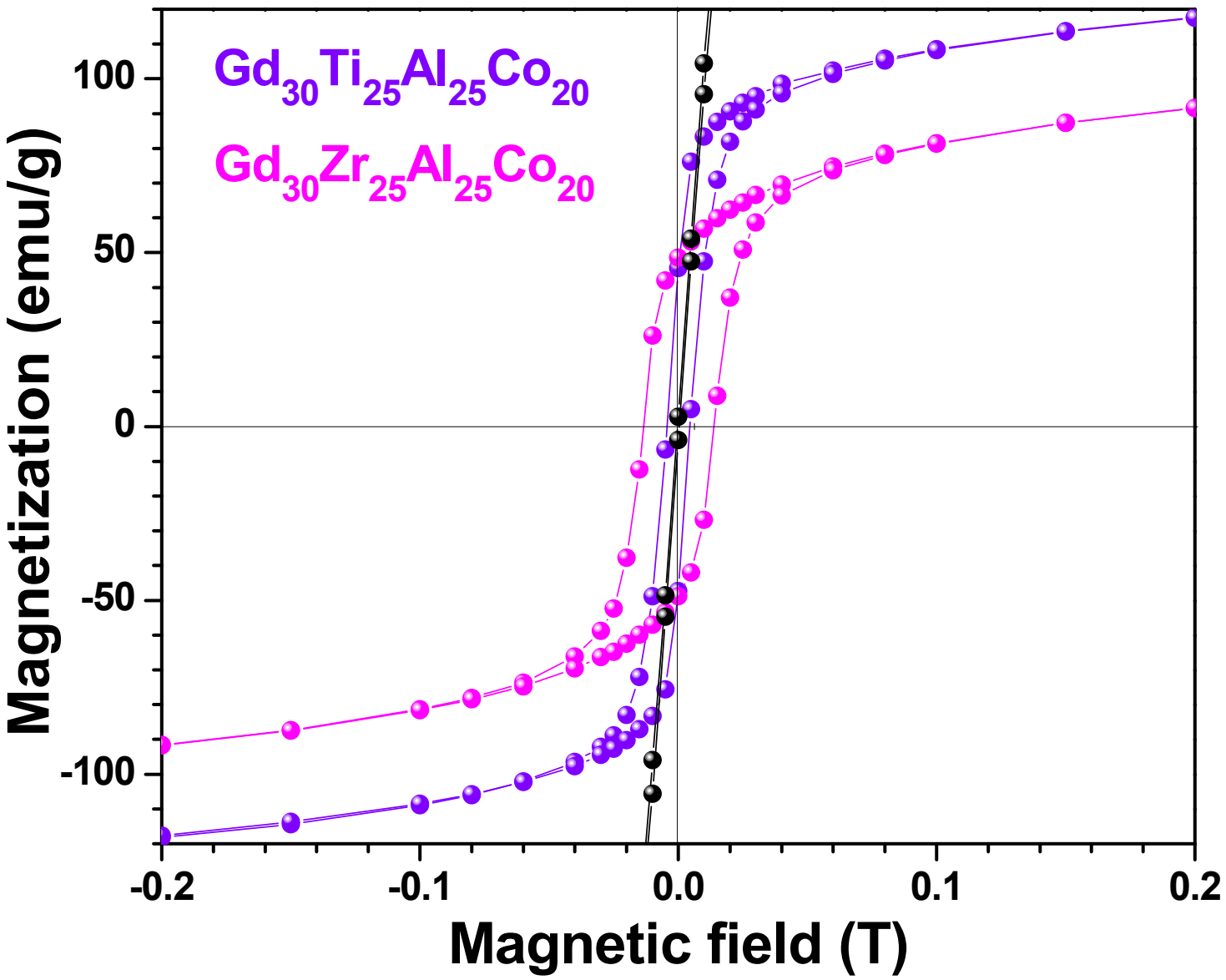
Gd30Ti25Al25Co20
Gd30Zr25Al25Co20
Magnetization (emu/g)
100
50
0
-50
-100
-0.2
-0.1
0.0
0.1
0.2
Magnetic field (T)

Interconnected structure

$Gd_{30}Zr_{25}Al_{25}Co_{20}$

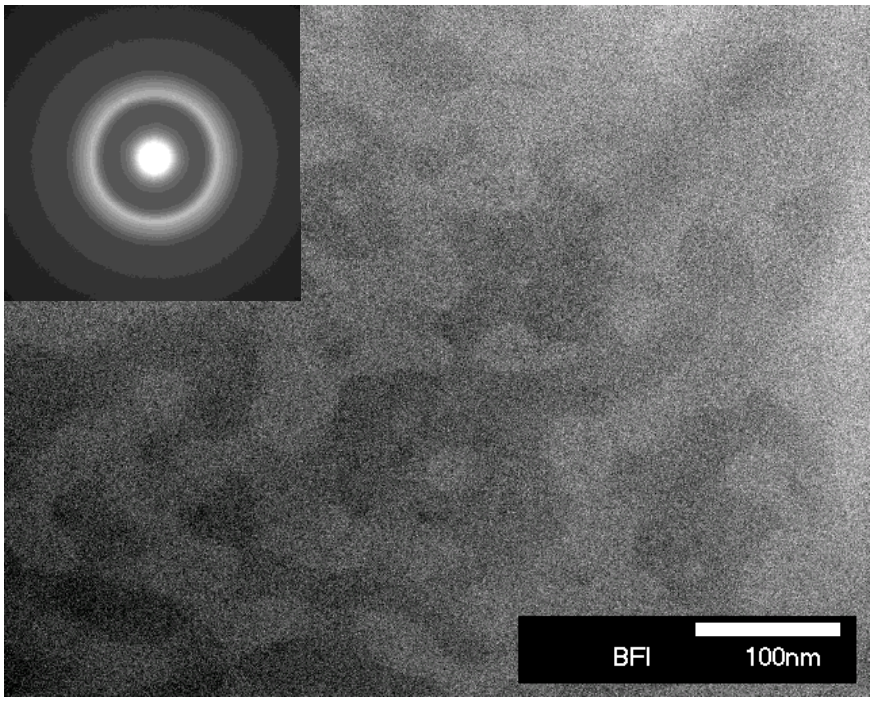

Amorphous + Amorphous

$Gd_{30}Zr_{25}Al_{25}Cu_{20}$

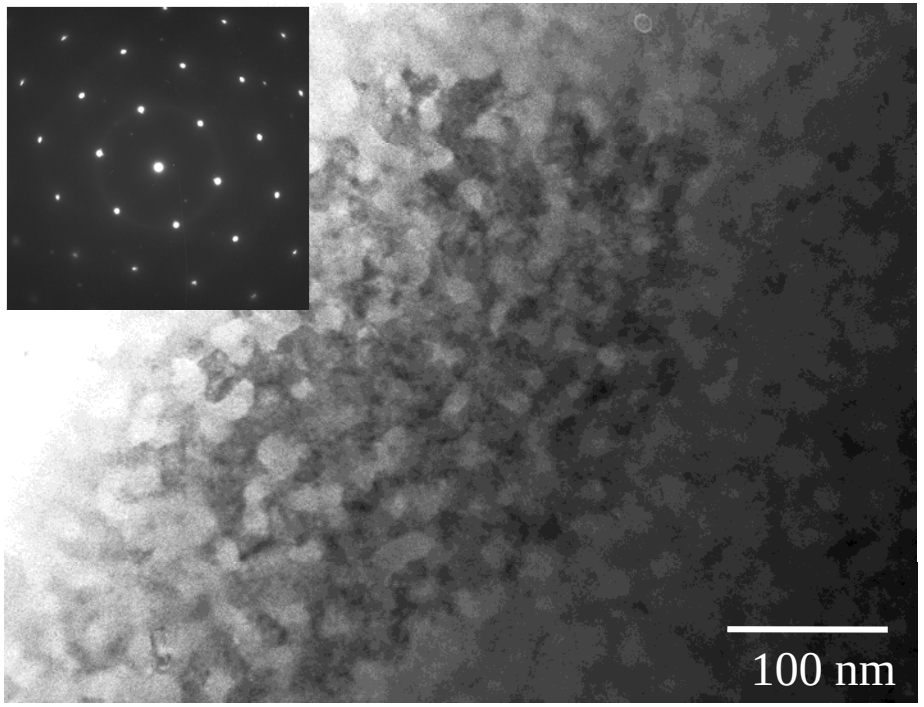

Amorphous + Crystals

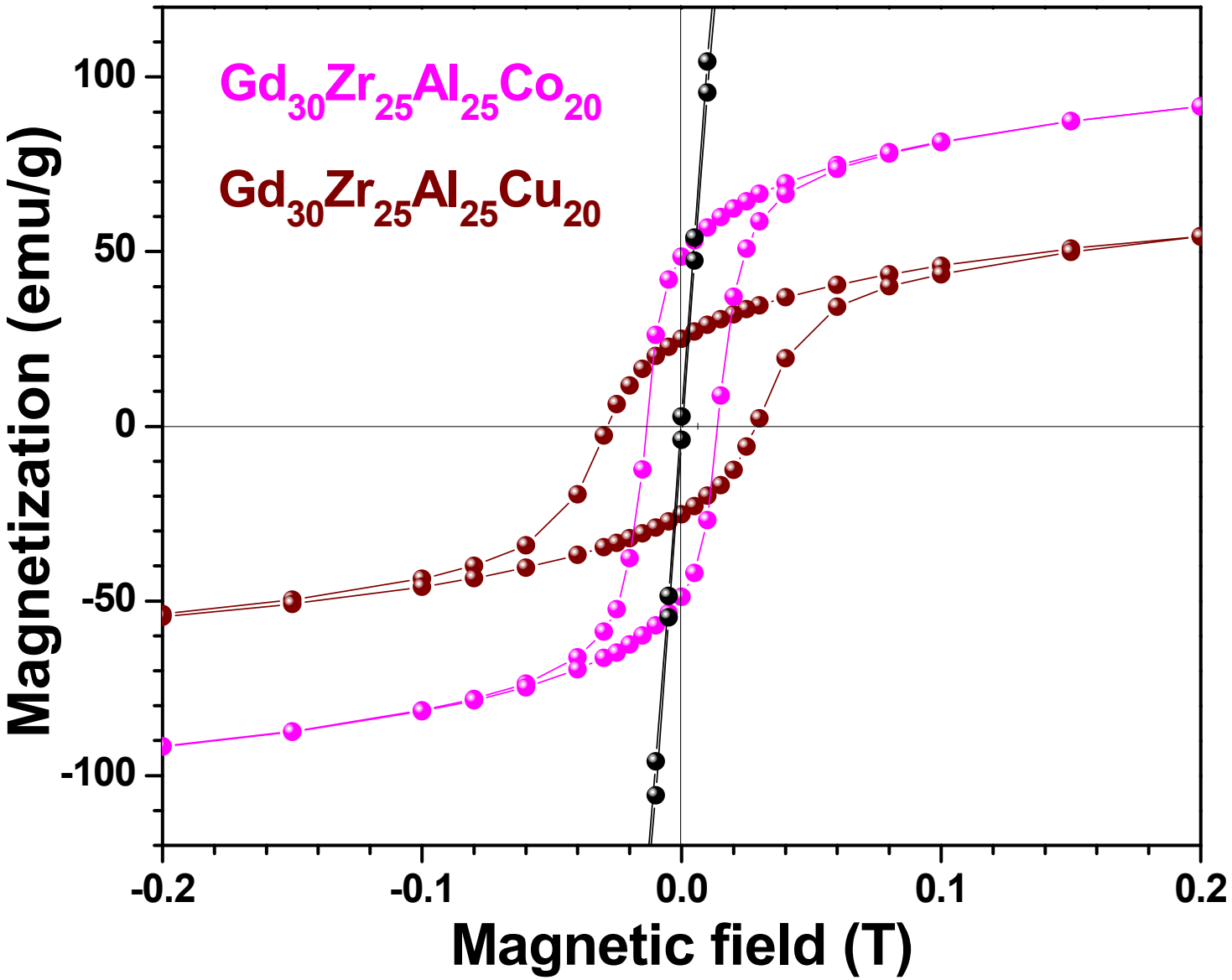
Gd30Zr25Al25Co20
Gd30Zr25Al25Cu20
Magnetization (emu/g)
Magnetic field (T)
100
50
0
-50
-100
-0.2
-0.1
0.0
0.1
0.2

$Gd_{30}Zr_{25}Al_{25}Co_{20}$

* unpublished (2007)

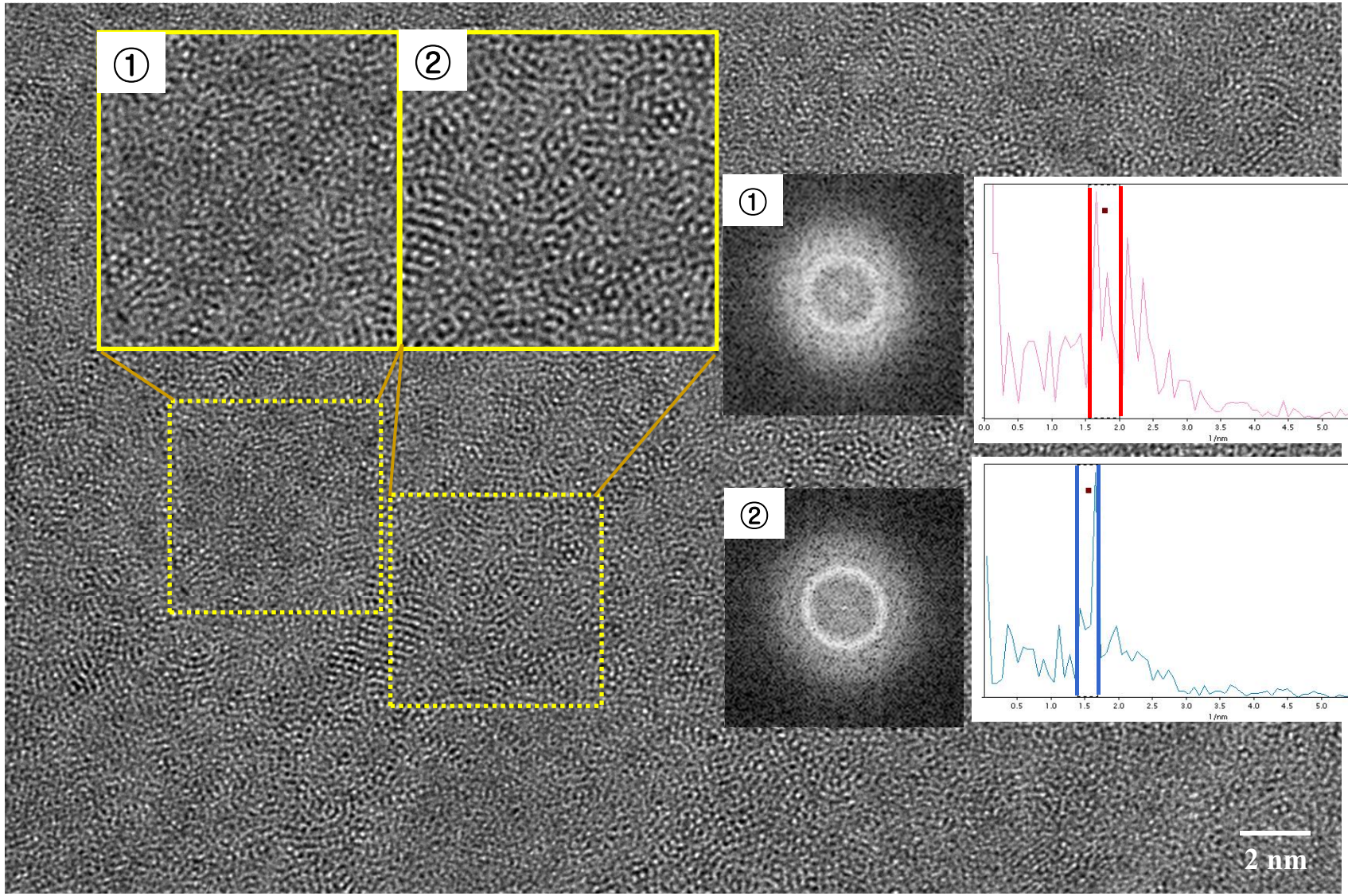

Effect of element with positive enthalpy of mixing among constituent elements

atomic scale heterogeneity

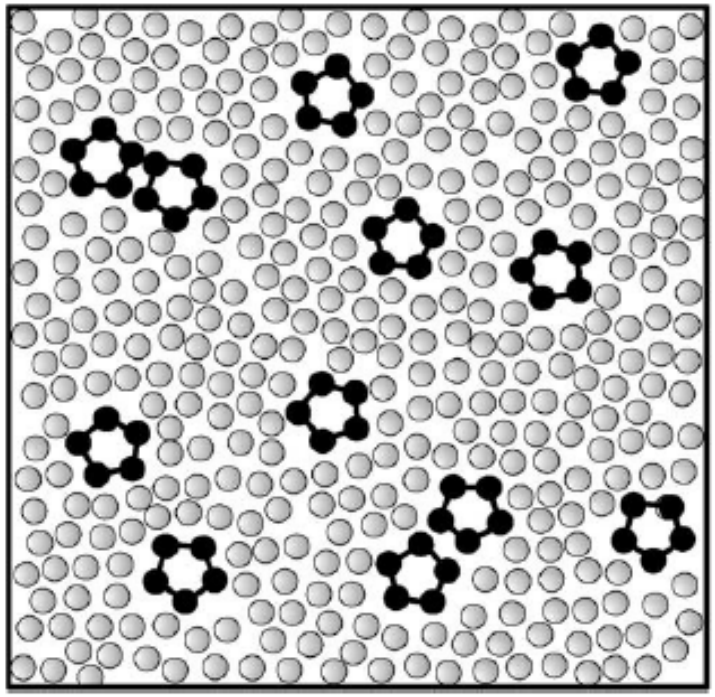

Enhancement of plasticity in BMGs

Phase separating metallic glasses

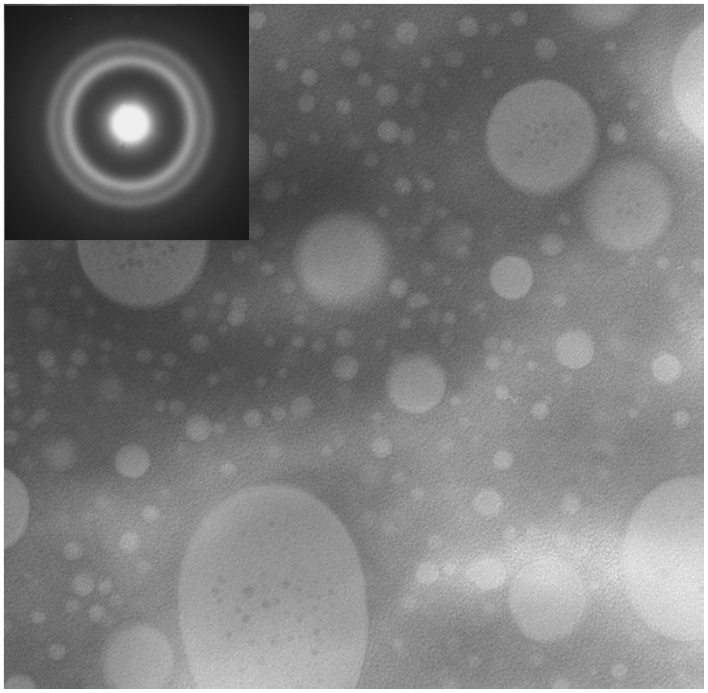

Unique properties

Dealloying (selective dissolution) process

- **Process of selective dissolution of the most electrochemically active component**

J. Jayaraj et al., Scripta Mat., 55 (2006) 1063.

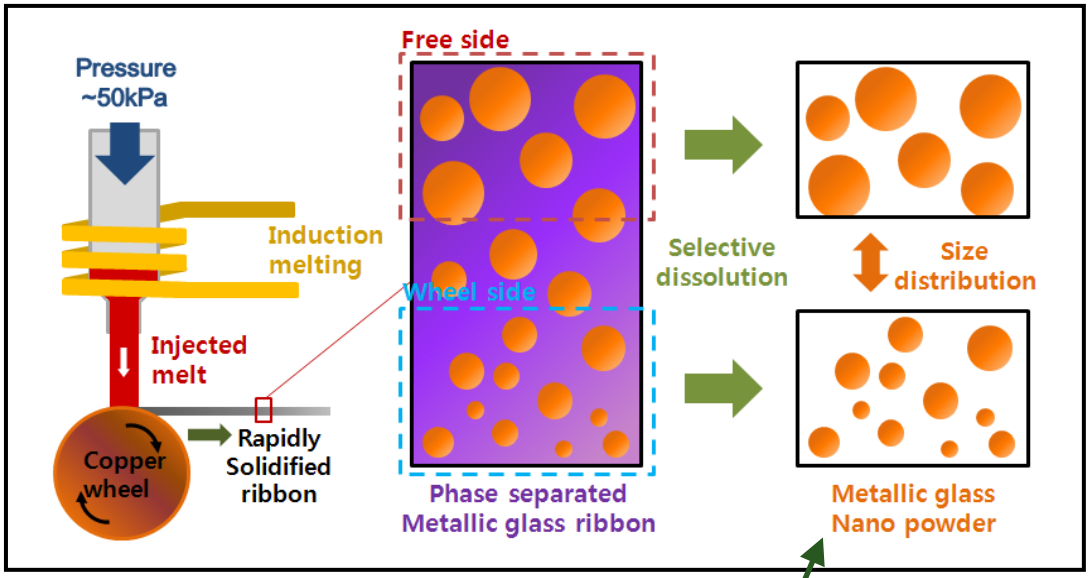

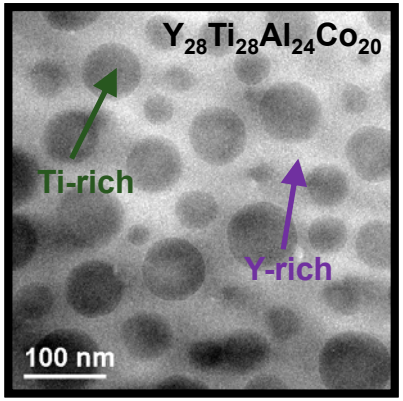

Dealloying process

J. Jayaraj et al., Scripta Mat., 55 (2006) 1063.

Y : intensively reactive to HNO_3 soln.
Ti : strong resistance to corrosion by HNO_3 soln.

Immersion of the alloy in etchant solution.

➡ Selective dissolution of Y-rich phase

➡ Formation of Ti-rich spherical nanoparticles

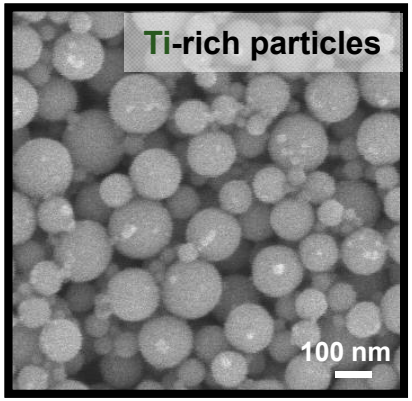

Selective dissolution of Y-rich phase

- Immersion of $Y_{28}Ti_{28}Al_{24}Co_{20}$ alloy in 0.1M HNO_3 for 24hrs

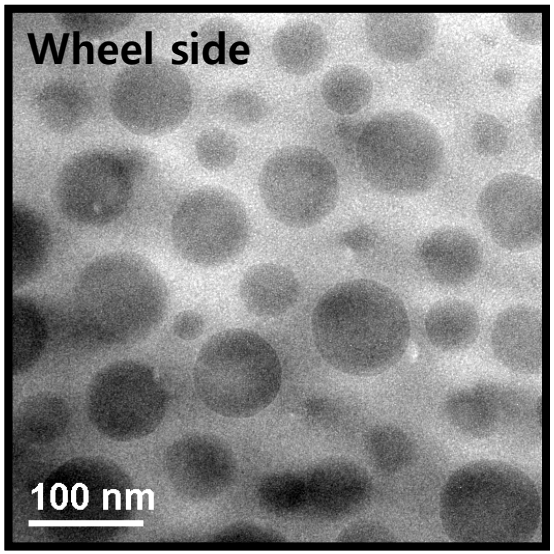

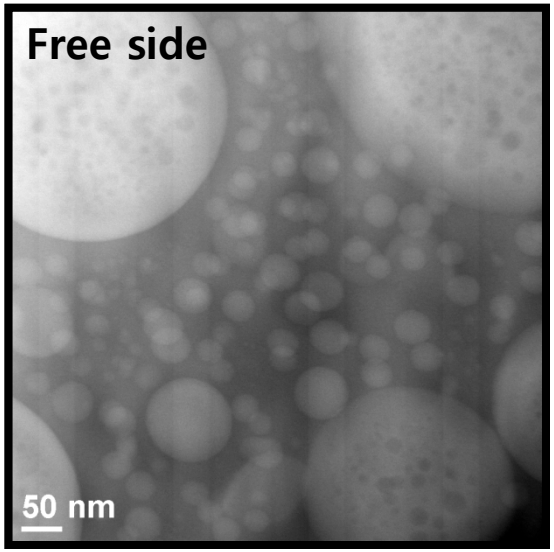

$Ti + 2H_2O \rightarrow TiO_2 + 2H_2$: passivation by TiO_2

$2Y + 6H^+ \rightarrow 2Y^{3+} + 3H_2$: Ionization

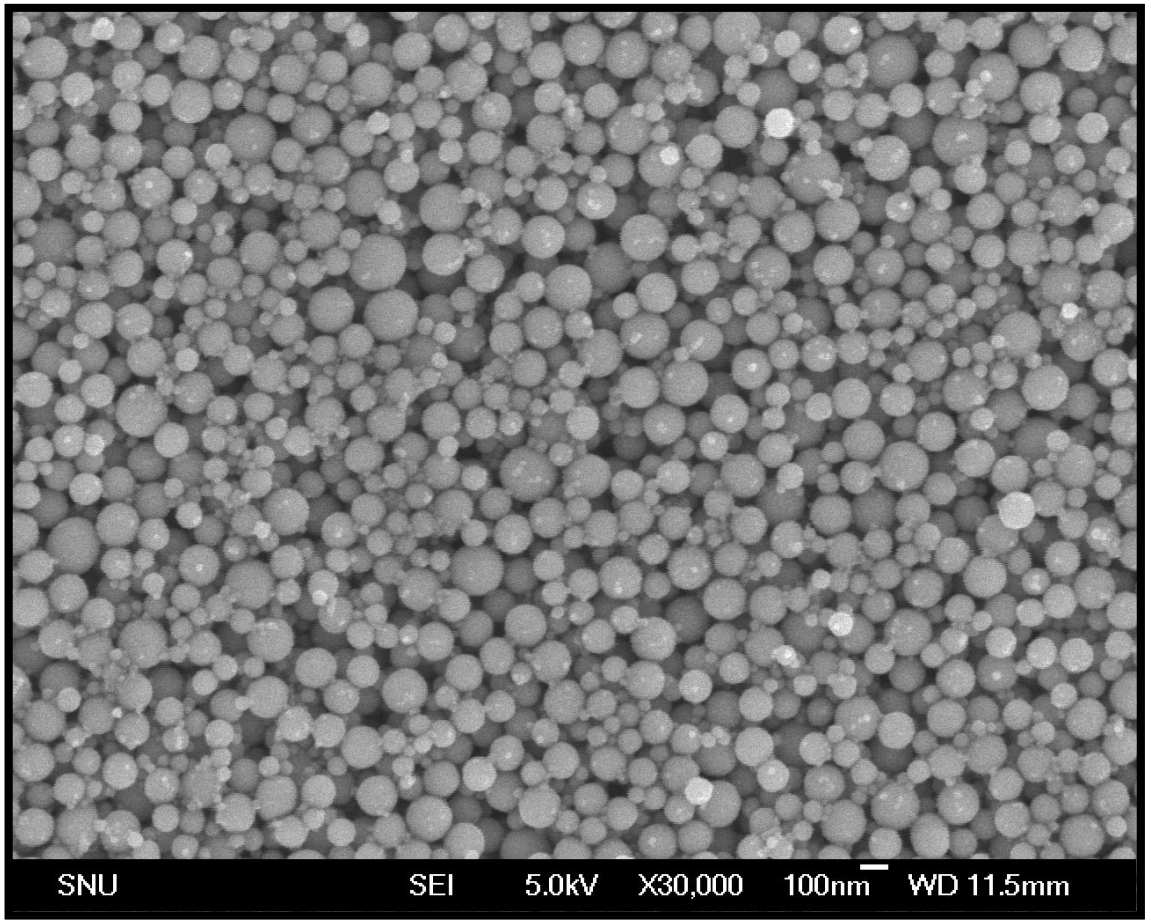

Co-rich region formation after oxidation

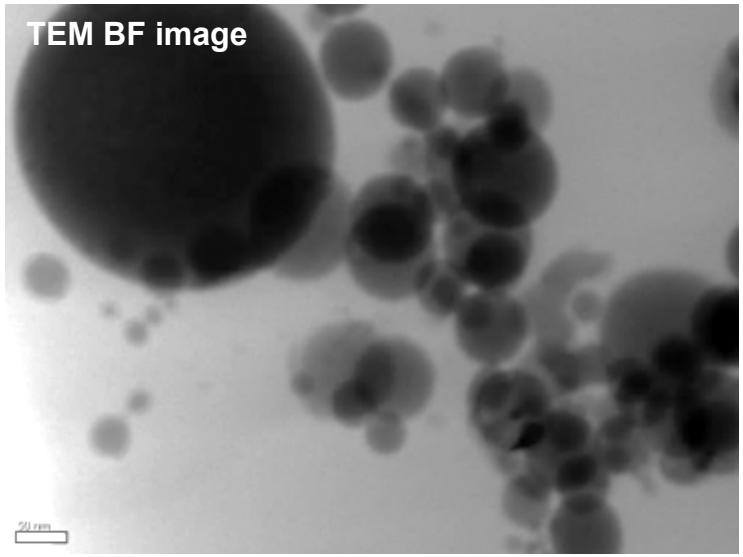

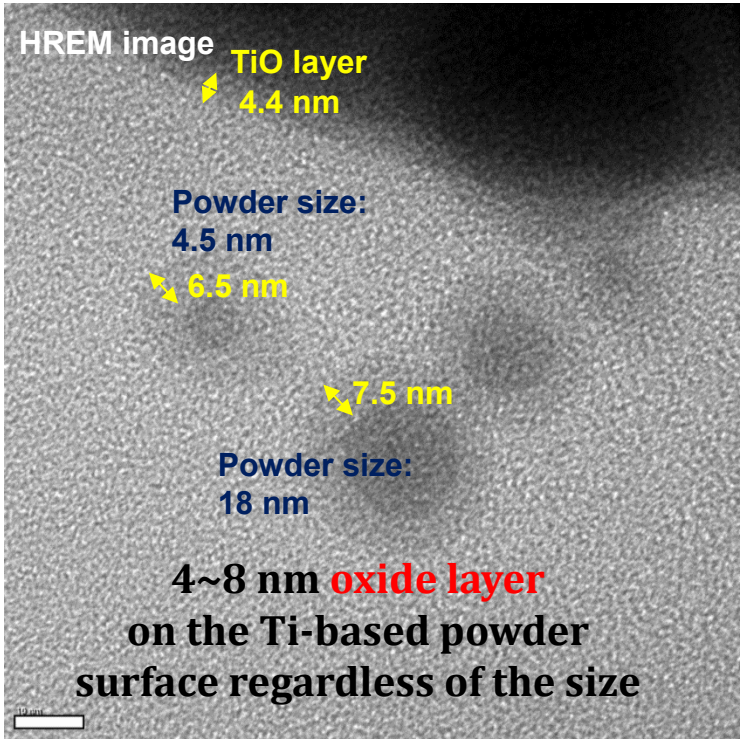

4~8 nm oxide layer on the Ti-based powder surface regardless of the size

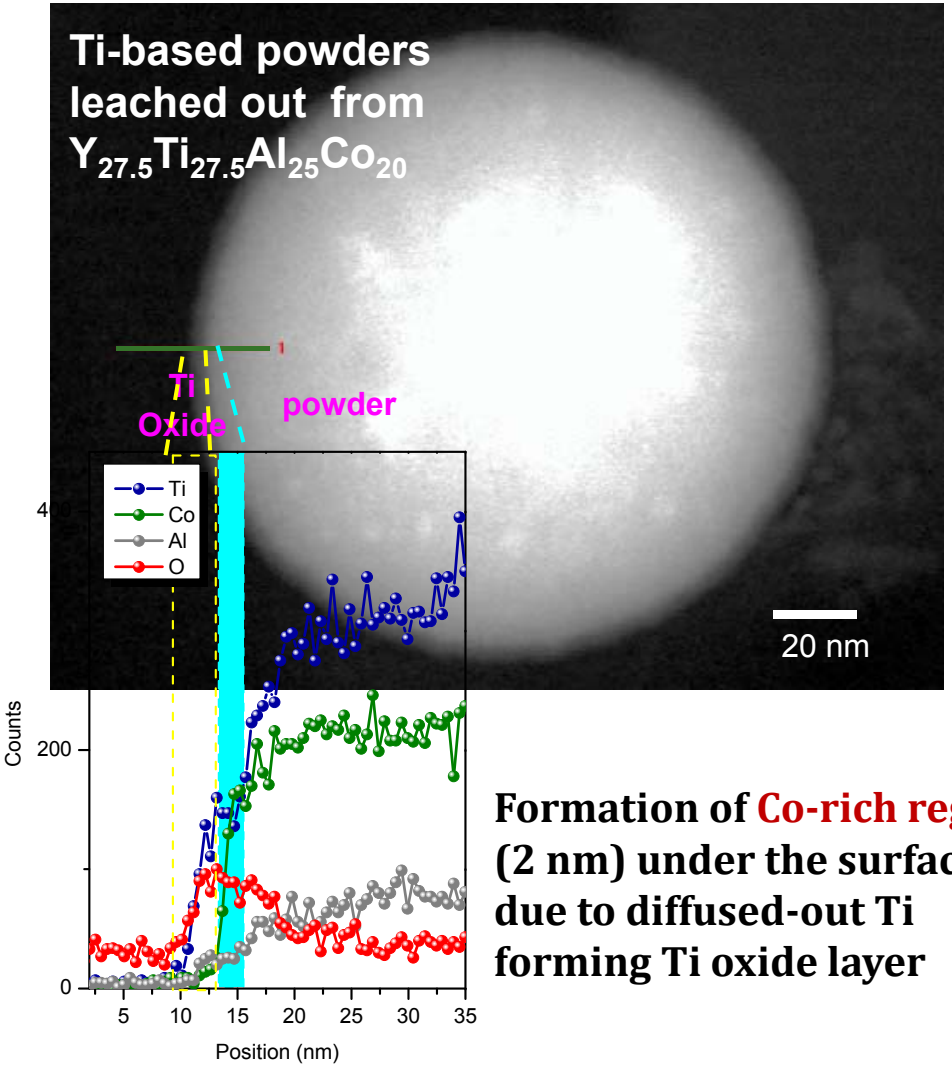

Formation of Co-rich region (2 nm) under the surface due to diffused-out Ti forming Ti oxide layer

Oxide layer	Co-rich region (Ave. comp.)	Particle (Ave. comp.)
Ti-O	$Ti_{16}Co_{22}Al_4O_{58}$	$Ti_{51}Co_{38}Al_{11}$

Surface modification of Ti-based nanopowders ➡ unique properties

▸ **SQUID results**

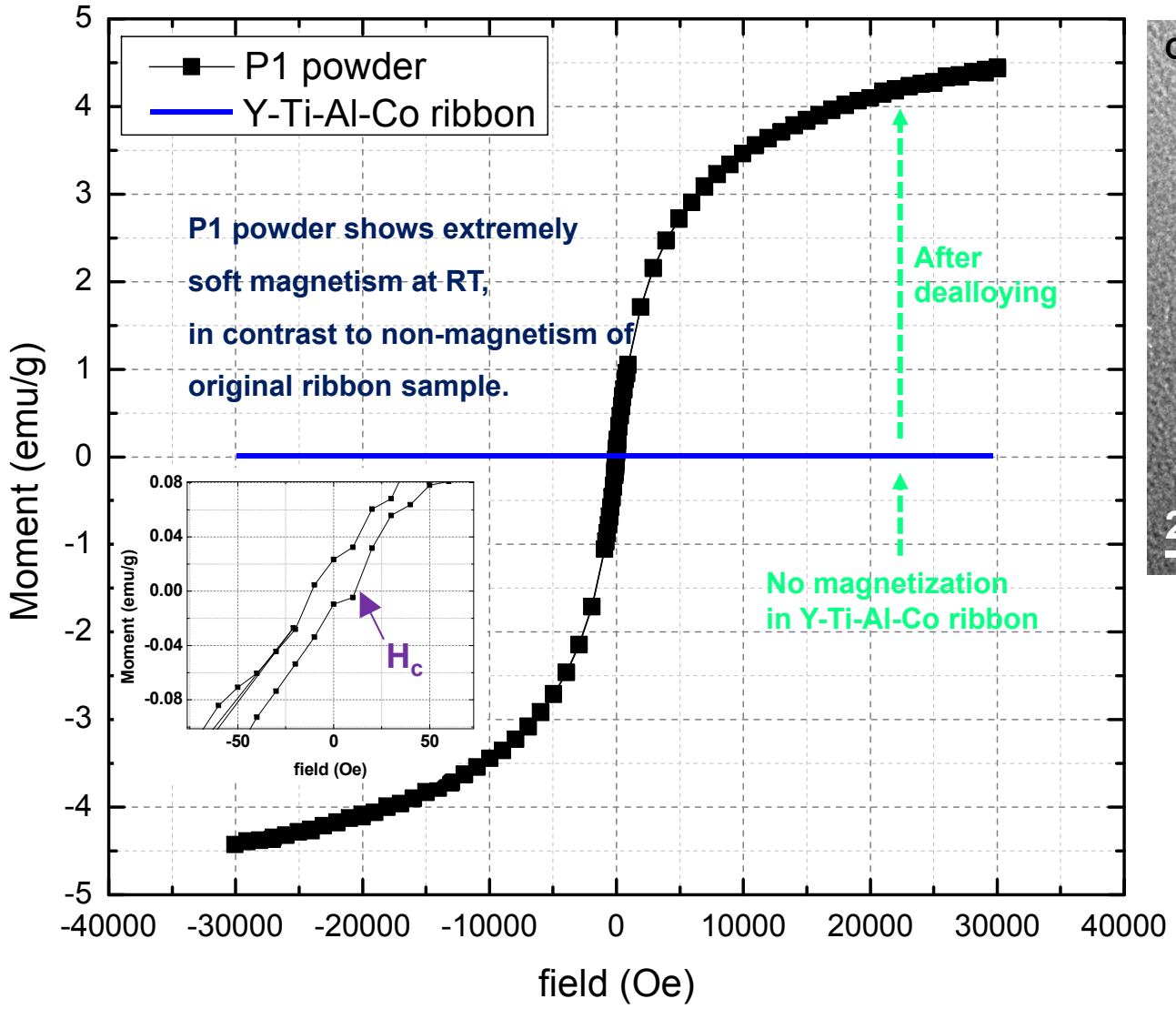

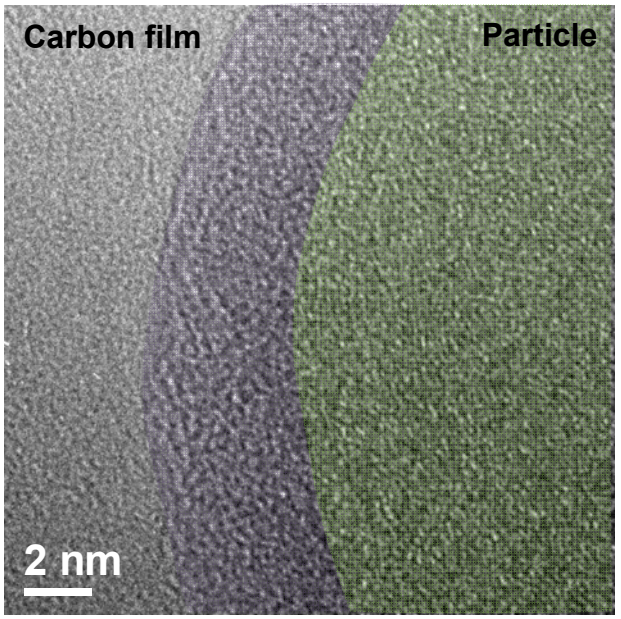

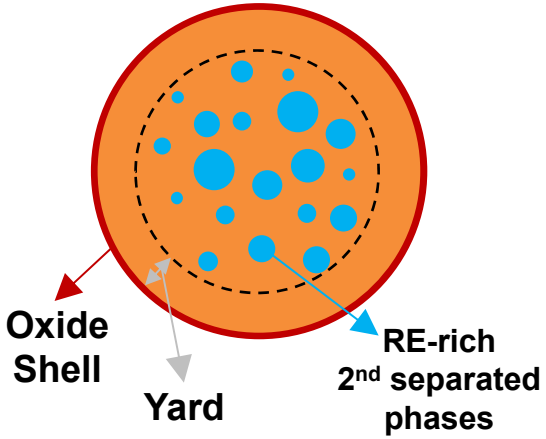

Selective dissolution of Ti-rich phase

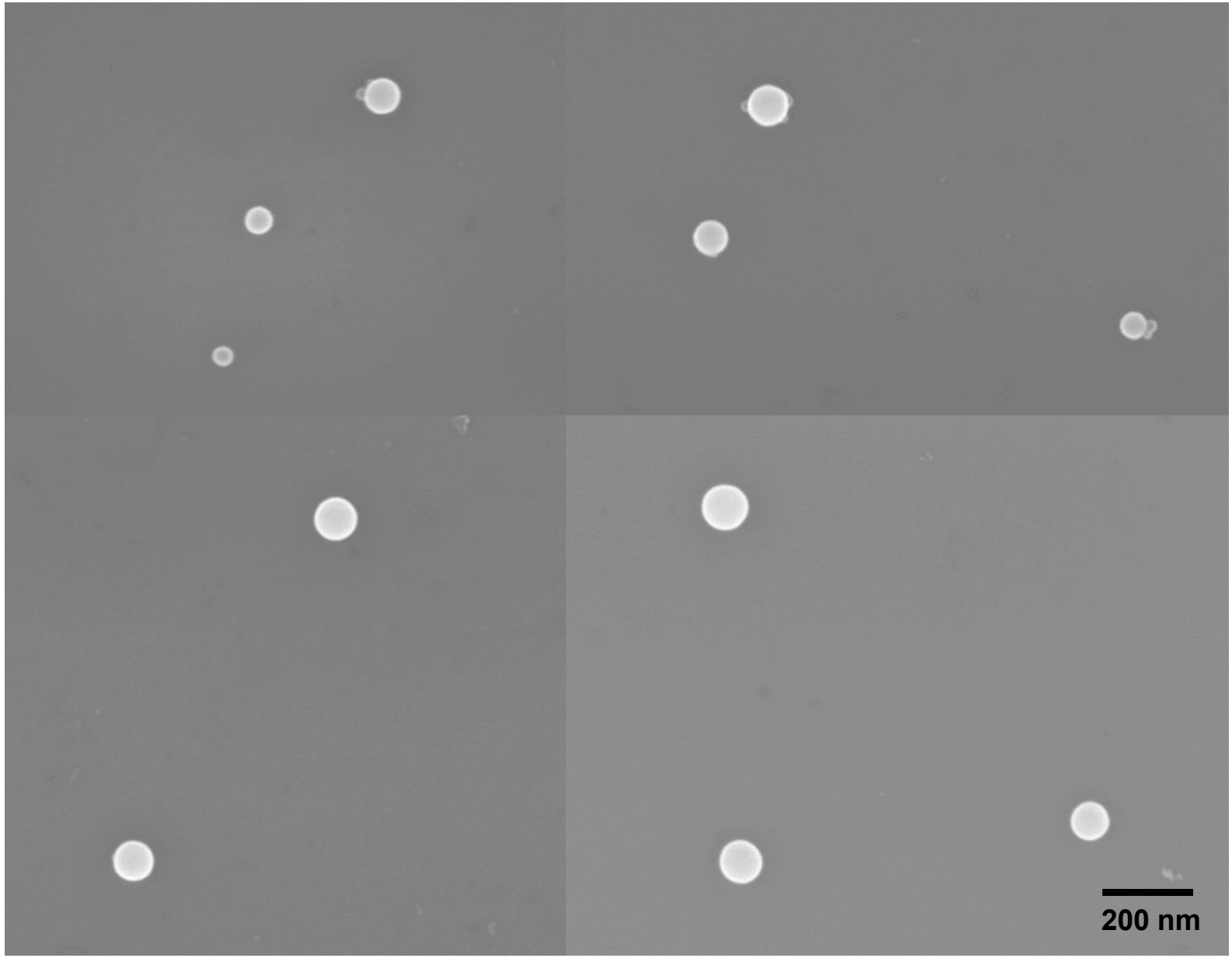

Hysitron Picoindenter PI-85 (for SEM) & PI-95 (for TEM)

PI-85 with FEI FE-SEM

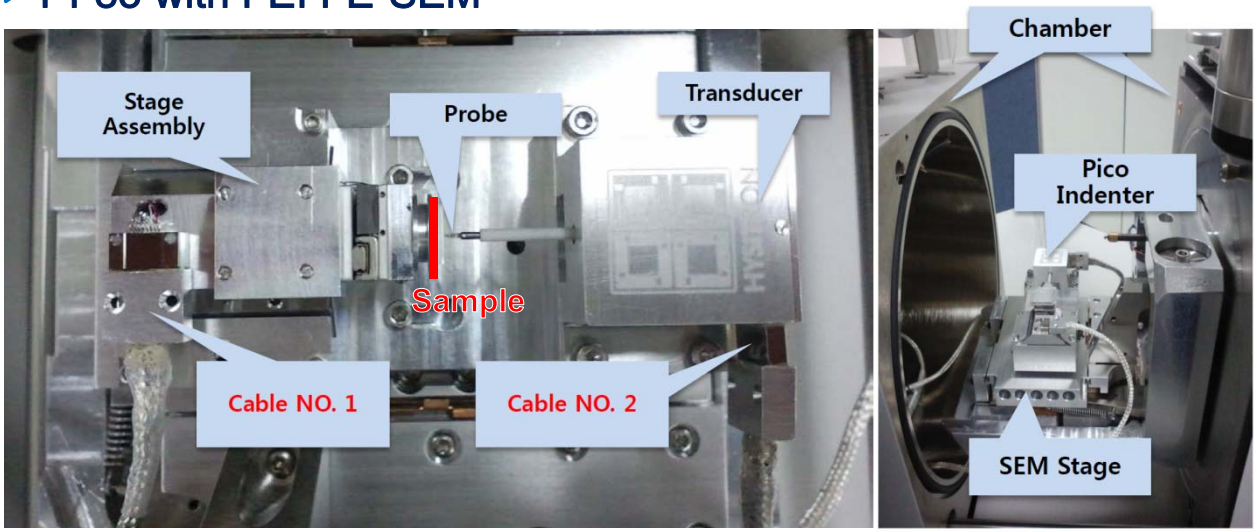

☐ Pico Indenter + SEM Chamber

PI-95 for FEI TEMs (F20, Titan)

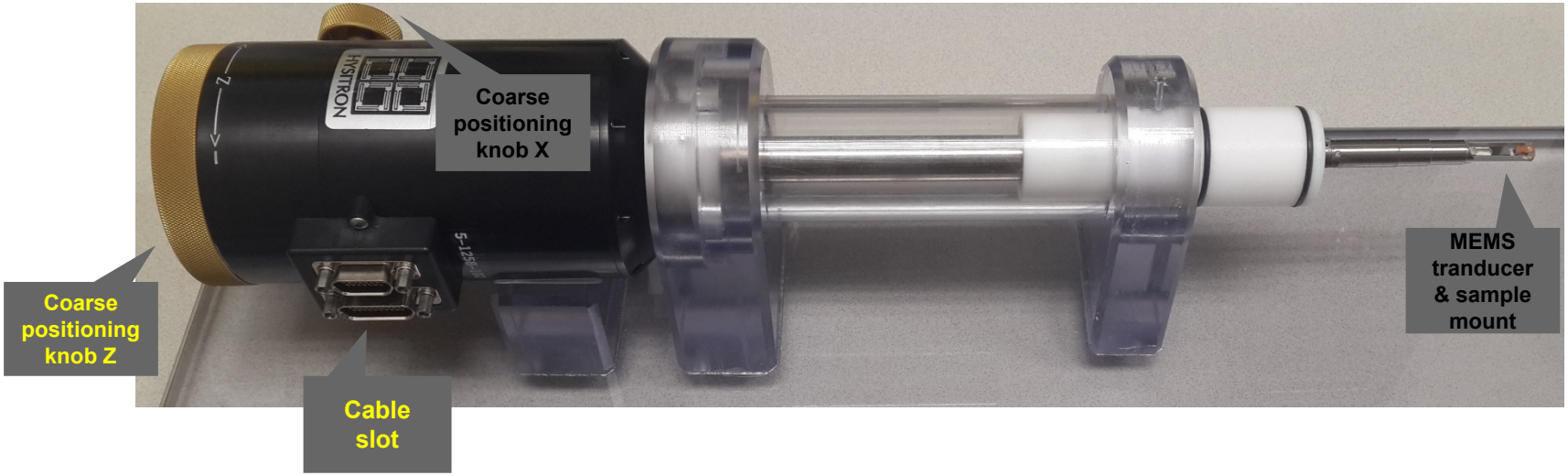

Movie of in-situ compression test using pico-indenter

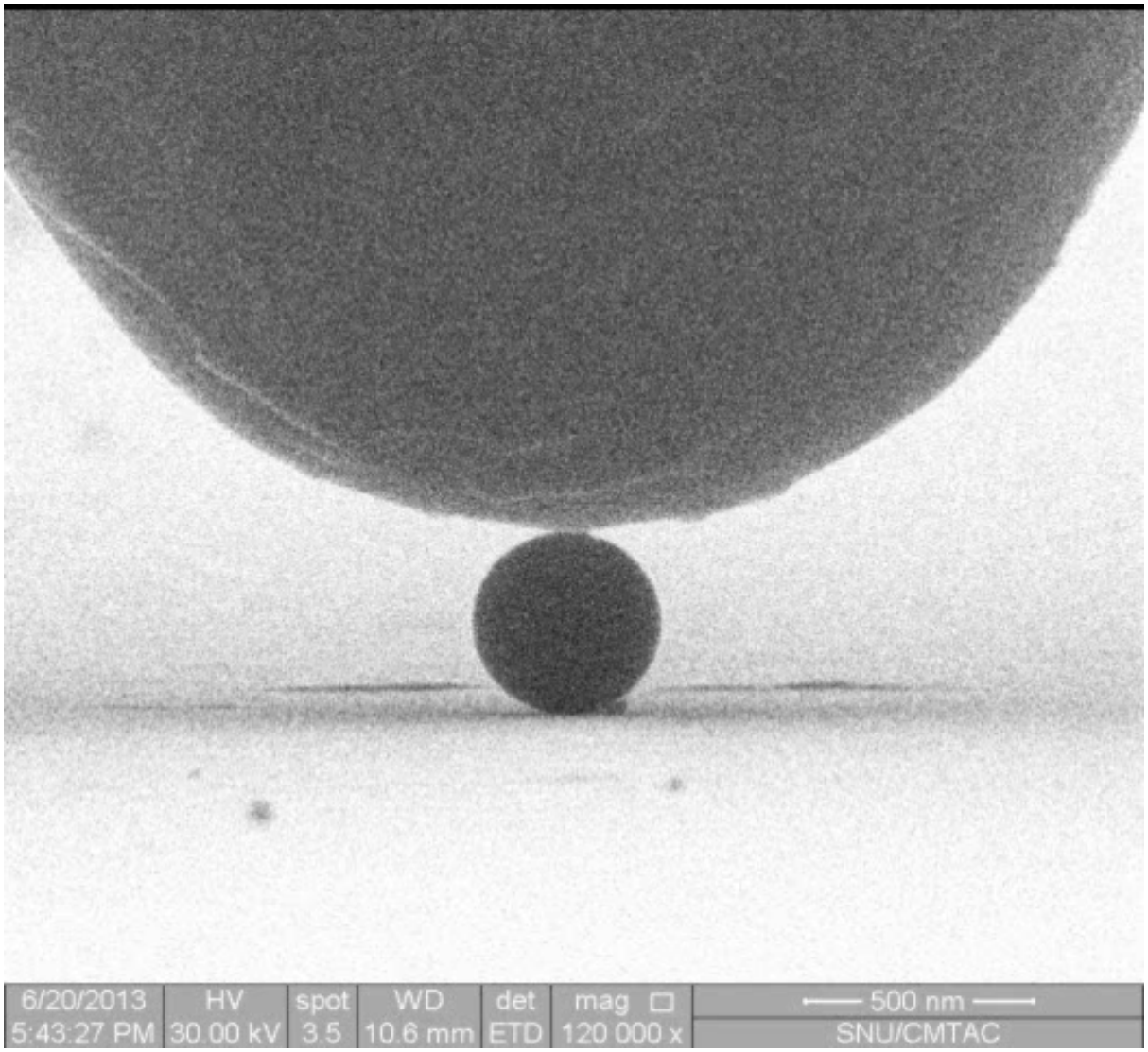

Particle images before & after compression test using pico-indenter

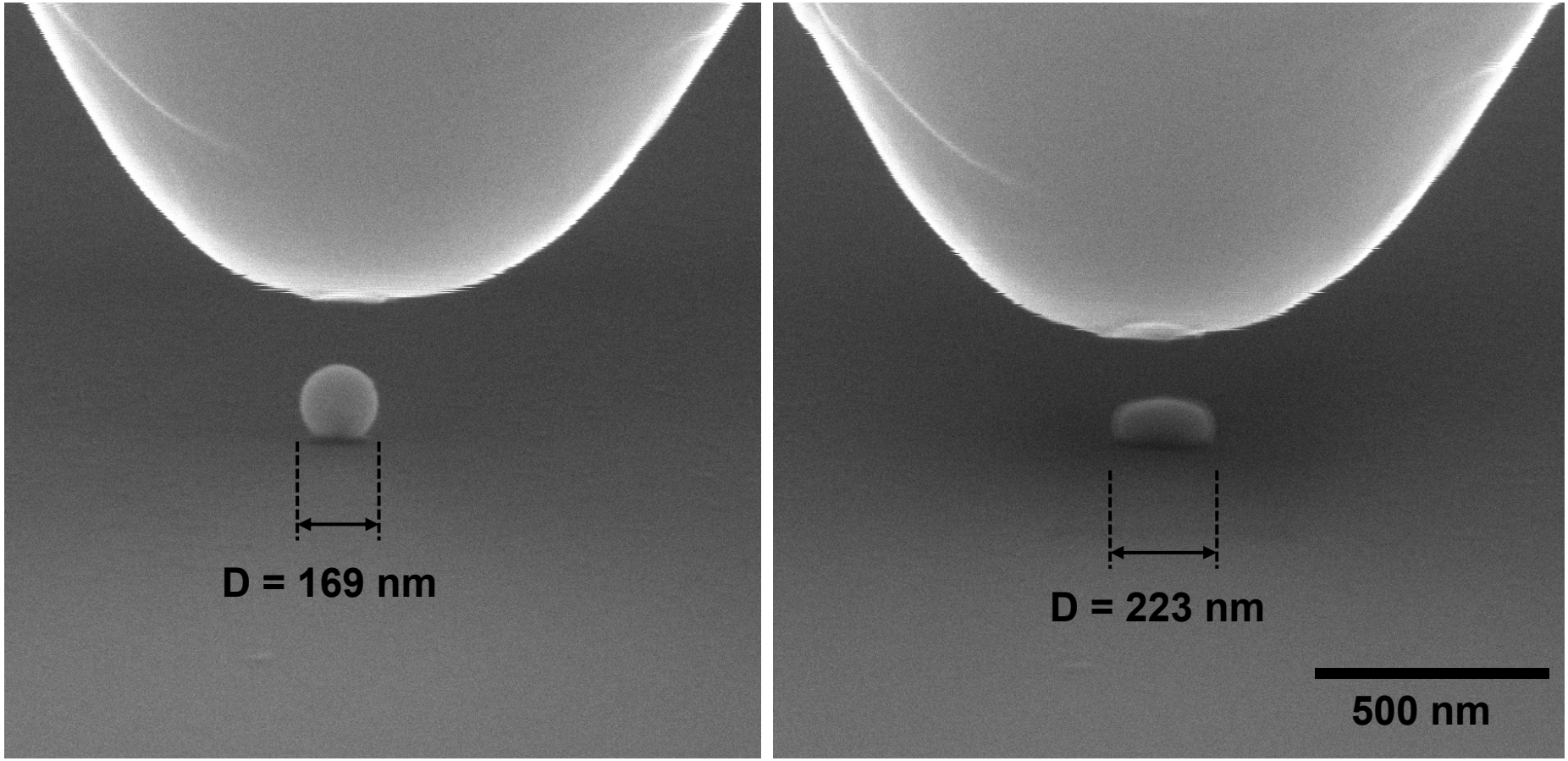

5.7.4 Crystallization: T_x ~ kinetic temperature, depends on the heating rate

- The nature of the crystalline phase produced on long time annealing was different depending on whether the annealing temperature was below Tg or above Tg.

→ In the glass state, the number of crystalline nuclei is constant, while in the supercooled liquid state, the nucleation rate is constant. In both the cases, the crystal nuclei grow through an interfacial reaction controlling process.

$$f = 1 - \exp\left(-kt^n\right)$$

k: 온도에 민감 $f(I, v)$ $\quad -\frac{\pi}{3} I v^3$

n: 1 ~ 4 (depend on nucleation mecnanism)

Growth controlled. Nucleation-controlled.

n value is not constant, but is increasing continuously from 3.0 to 3.7 with increasing T_a.

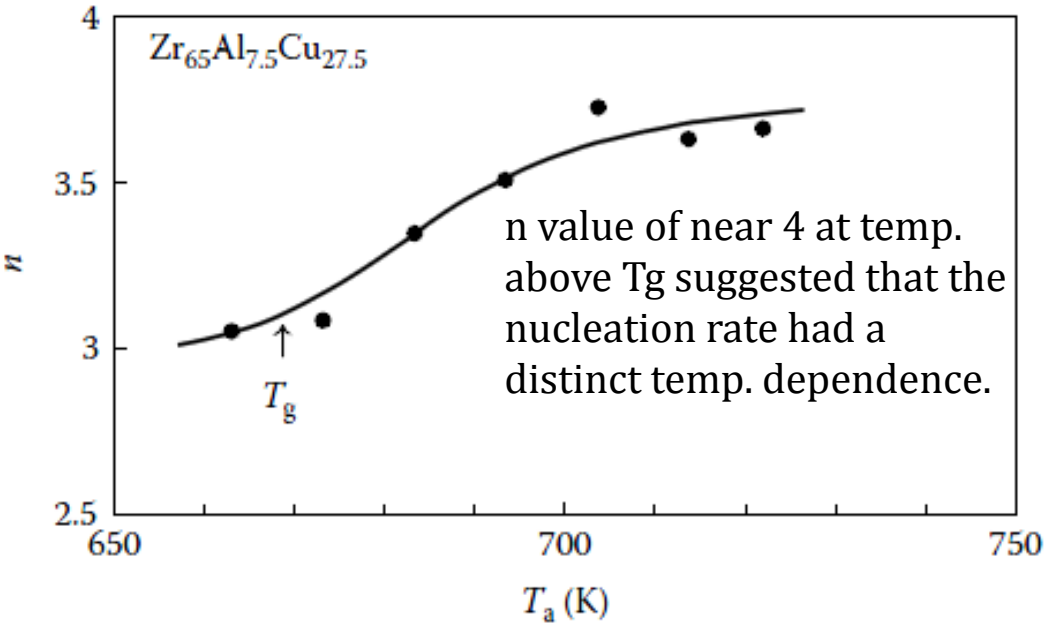

FIGURE 5.21
Variation of the Avrami exponent, n with annealing temperature, T_a during the isothermal annealing of glassy $Zr_{65}Al_{7.5}Cu_{27.5}$ alloy.

The nucleation rate is a function of both t_a and T_a. For isothermal annealing, the nucleation rate, $I(t_a)$ as a function of annealing time, t_a, at any temperature can be expressed according to the equation

$$I(t_a) = I_0 \exp\left(-\frac{\tau}{t_a}\right) \tag{5.9}$$

where

I_0 is the steady-state homogeneous nucleation rate

τ is the incubation time

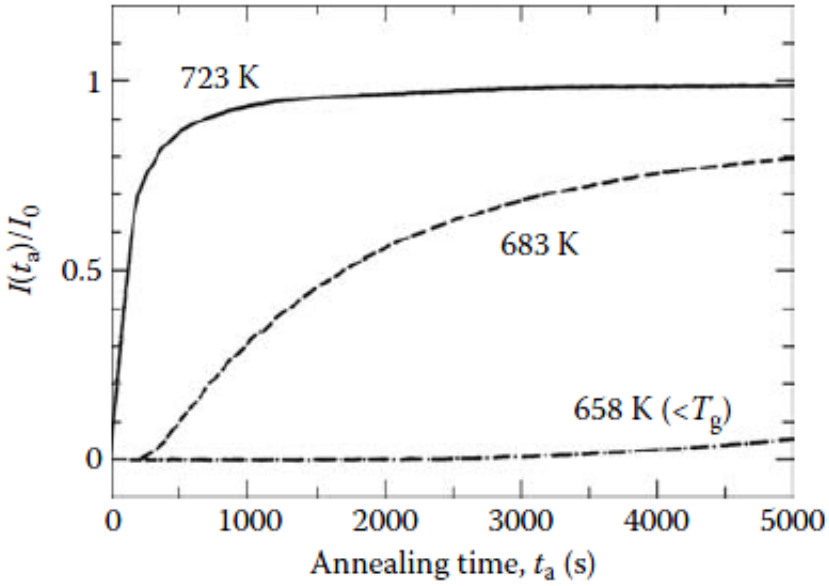

FIGURE 5.22
Variation of the reduced homogeneous nucleation rate, $I(t_a)/I_0$ evaluated from the incubation time for the precipitation of the $Zr_2(Cu,Al)$ phase with annealing time, t_a for the glassy $Zr_{65}Al_{7.5}Cu_{27.5}$ alloy annealed at 658, 683, and 723 K.

* **Non-Arrehenius-type thermal activation process**: The activation energy was calculated to change from 400 kJ/mol in the glassy solid to 260 kJ/mol in the supercooled liquid state for the nucleation of the Zr_2Cu and ZrAl phases, and from 370 kJ/mol in the glassy solid to 230 kJ/mol in the supercooled liquid state for crystallization.

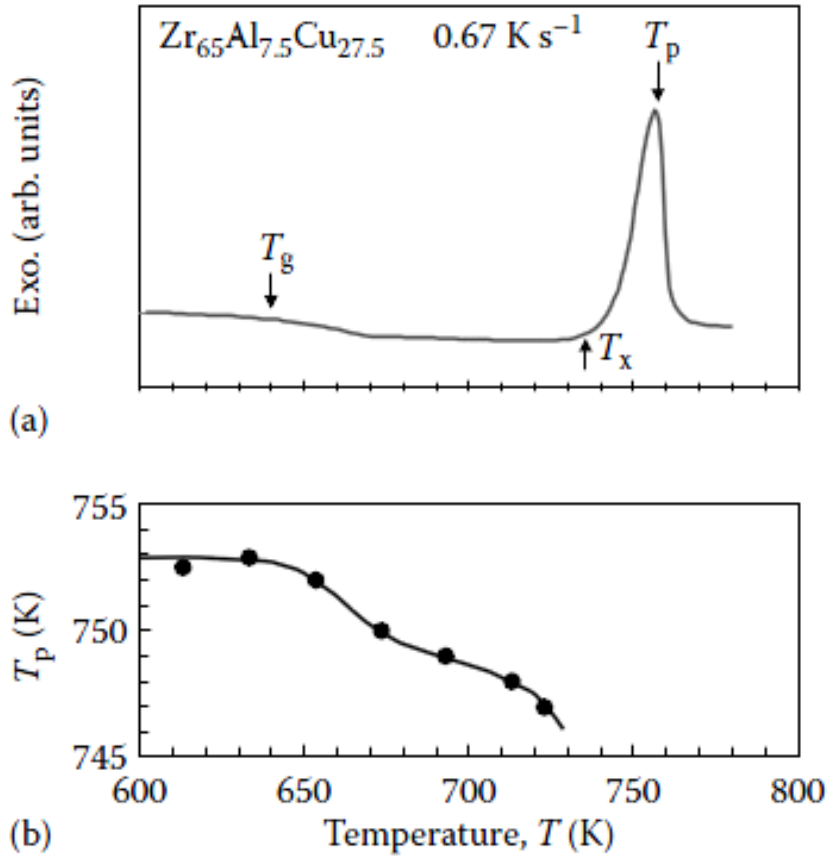

FIGURE 5.23
(a) DSC plot of the $Zr_{65}Al_{7.5}Cu_{27.5}$ glassy alloy continuously heated at a rate of 0.67 K s^{-1} (40 K min^{-1}). The T_g, T_x, and T_p values are indicated. (b) Variation of the peak temperature, T_p in the exothermic reaction due to crystallization with heating temperature, T_a.

* **The peak temperatures for nucleation and growth are well separated for glassy alloys exhibiting a significant width of the supercooled liquid region (ΔTx)**, where as for glassy alloys that do not show a Tg, these two peak temperatures overlap. This difference is expected **to reflect in the nature of the crystallized product** obtained from the supercooled liquid region. Accordingly, **the crystallized structure was examined as a function of the heating rate.**

---

* In $Zr_{65}Al_{7.5}Cu_{27.5}$ with large ΔTx, the contribution to the growth rate increases with increasing heating rate as compared with the contribution to the nucleation rate. However, no significant change in the grain size of the Zr_2Cu phase with heating rate is seen for the $Zr_{67}Cu_{33}$ alloy with the much smaller ΔTx.

→ **Thus, the increase in the contribution to the growth rate with increasing heating rate becomes significant at temperatures just below Tx in the wide supercooled liquid region.**

- **Annealed for 1020s (17min) at 693K (above Tg): BCT Zr2Cu phase precipitated in SCLR**/ dendritic morphology with a preferential growth direction, indicating that the redistribution of the constituent elements at the liquid-solid interface was necessary for the growth of the crystalline phase.
- **Annealed for 780 ks (9 days) at 613 K (below Tg): Zr2Cu phase precipitated in the glassy solid**/ a nearly spherical morphology with rather smooth interface, suggesting that the growth of the Zr2Cu phase took place in the absence of significant redistribution of the constituent elements at the interface between Zr2Cu and the glassy phases/ more homogeneous distribution of Zr2Cu

---

* **The structure and morphology of the crystallized phases also appear to be a function of the Al content in the alloy.**

5.8 Effect of Environment: especially in the case of reactive glasses, for example, those based on Zr and Fe.

- In $Fe_{77}Gd_3B_{20}$ ribbon, the significant difference in the crystallization behavior was attributed to **surface oxidation, which reduces their thermal stability.**

- In $Zr_{41}Ti_{14}Cu_{12.5}Ni_{10}Be_{22.5}$, the crystallization of the glassy phase started earlier with decreasing air pressure during annealing due to deeper oxygen penetration at low pressure./ Oxygen is know to speed up the crystallization process by promoting extra heterogeneous sites for nucleation. When the oxygen pressure was low , the thickness of the surface oxide layer was small and therefore more oxygen could diffuse inside and accelerate the crystallization process.
  → The crystallization kinetics were faster at low partial pressure of oxygen.

- **The presence of oxygen in the alloys has a significant effect on the nature of the phases formed after quenching and also those formed on crystallization.** Therefore, it is essential that the alloys are clean and devoid of impurities, especially in active metals. Otherwise comparison between results by different investigators becomes difficult.

5.9 Effect of Pressure during Annealing

- hot pressing, hot extrusion, hot isostatic pressing, and other recently developed methods such as spark plasma sintering
- becomes useful to evaluate the thermal stability of glasses when exposed to high pressures
- critical for optimizing the consolidation process parameter or deforming in the supercooled liquid region

* Four different effects of pressure during annealing

1. Since there is an increase in the density of the product on crystallization (the glassy alloys are about 1%–2% less dense than their crystalline counterparts), it is natural to expect that the application of pressure would reduce the free volume in the glassy phase and therefore it is expected that crystallization will be accelerated. Such a process could easily happen when the glass crystallizes by a polymorphous mode.
2. Due to the retarded mobility of atoms (diffusivity) under high pressures, atomic diffusion is reduced and therefore crystallization is retarded as evidenced by the increase of crystallization temperatures. Since atomic diffusion is required for primary and eutectic-type crystallization modes, the application of pressure is expected to retard the crystallization of metallic glasses when the transformation takes place by any of these modes.

3. The relative Gibbs free energies of the glassy and other competing crystalline phases and also the activation barriers could be altered by the application of pressure. Consequently, metastable phases could form, the relative amounts of the different phases could be different, or alternately, different crystallization paths could be followed. The situation will be decided by the sign and magnitude of the variation of the crystallization temperature with pressure, that is, dT_x/dP.

   As an example, during the primary crystallization of Fe–B glassy alloys, α-Fe is formed at atmospheric pressure. However, when crystallization is conducted at pressures above 100 kbar, the formation of the metastable hcp ε-Fe phase was found to form [148]. Similarly, instead of the equilibrium tetragonal Nb_3Si phase, the cubic A15 Nb_3Si phase formed in the Nb–Si system during crystallization at high pressures in the glassy Nb–Si alloys [149]. Again, in the case of the crystallization of the $Zr_{41}Ti_{14}Cu_{12.5}Ni_{10}Be_{22.5}$ glassy alloy, Yang et al. [150] reported that the primary crystallized phase was the same at all pressures studied, but the subsequent phase-formation sequence was different at different temperatures.

4. The last effect of the application of pressure to metallic alloys is that amorphization could occur, that is, pressure-induced amorphization takes place [151–153]. For example, Wang et al. [151] reported that by cooling the $Zr_{41}Ti_{14}Cu_{12.5}Ni_{10}Be_{22.5}$ liquid at a high pressure of 6 GPa, they were able to obtain a high-density glassy alloy that had a structure and properties different from the low-density glassy alloy obtained by water quenching the melt.

TABLE 5.6

Effect of Pressure in Increasing the Crystallization Temperature of Bulk Metallic Glasses

Composition	Pressure Range Used (GPa)	Rate of Increase of T_x(K GPa^{-1})	Reference
$Al_{89}La_6Ni_5$	0–4	Decrease at a rate of 50 between 0 and 1 GPa and then increase at a rate of 25	[154]
$Fe_{72}P_{11}C_6Al_5B_4Ga_2$	0–2.4	30 (T_x dropped at higher pressures between 2.4 and 3.2)	[147]
$Mg_{60}Cu_{30}Y_{10}$	0–4	16	[155]
$Pd_{40}Ni_{40}P_{20}$	0–4.2	11	[156]
$Pd_{40}Cu_{30}Ni_{10}P_{20}$	0–4	11	[157]
$Zr_{66.7}Pd_{33.3}$	0–4	22	[135]
$Zr_{70}Pd_{30}$	0–3	11 ± 3 for quasicrystalline phase 9 ± 4 for intermetallic phase	[158]
$Zr_{65}Al_{7.5}Ni_{10}Cu_{7.5}Ag_{10}$	0–4.2	9.4 for T_{x1} No change for T_{x2}	[159]
$Zr_{48}Nb_8Cu_{14}Ni_{12}Be_{18}$	0–4.4	9.5	[160]
$Zr_{41.2}Ti_{13.8}Cu_{12.5}Ni_{10}Be_{22.5}$	0–3	19	[161]
$Zr_{46.8}Ti_{8.2}Cu_{7.5}Ni_{10}Be_{27.5}$	0–4.2	1.7	[162]
$Zr_{41}Ti_{14}Cu_{12.5}Ni_{10}Be_{22.5}$	0.5–6.5	12.8 (a sudden drop occurred at 5.6 GPa)	[150]

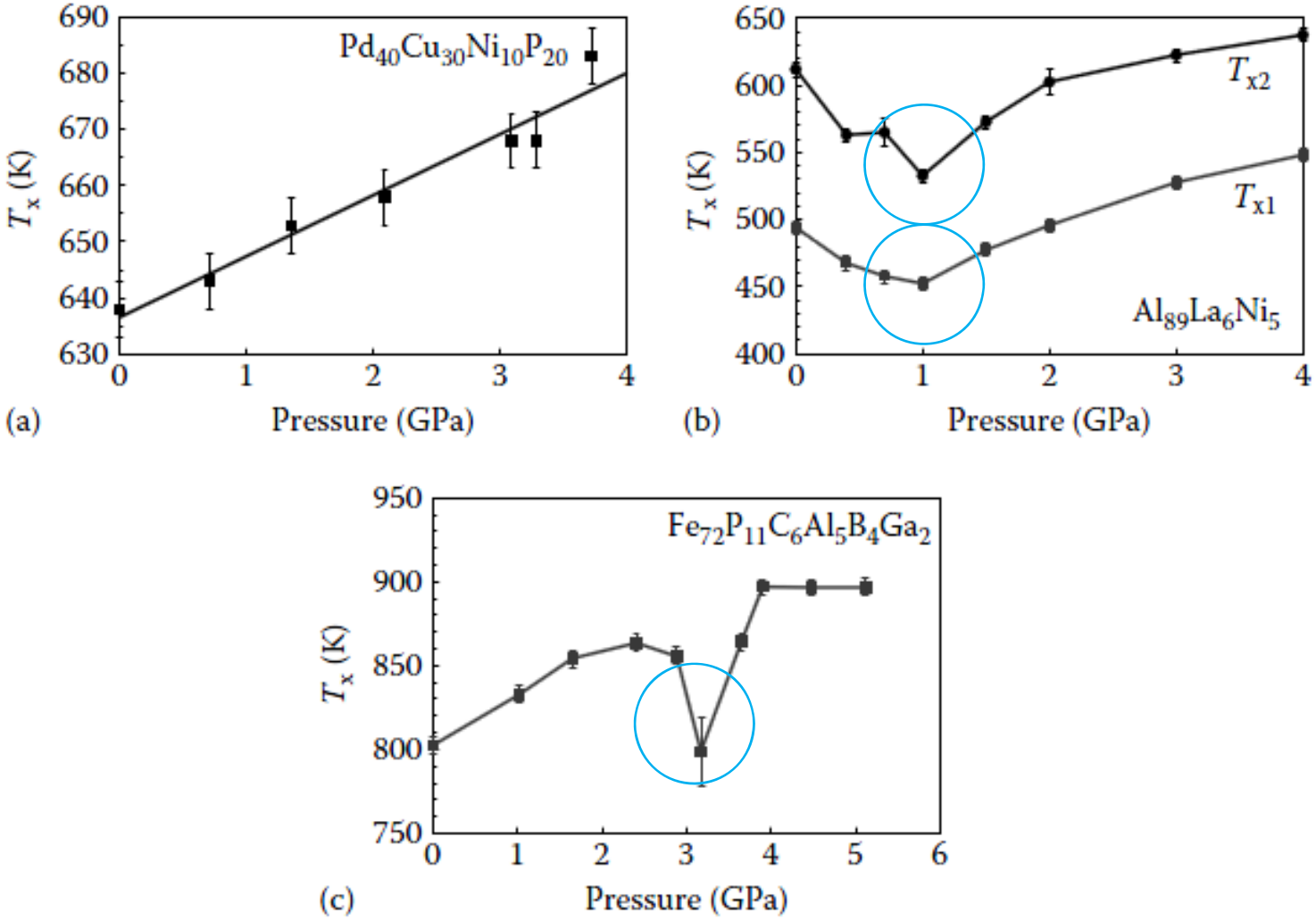

FIGURE 5.24
Variation of T_x with pressure in bulk metallic glassy alloys. Note that the T_x usually increases with increasing pressure although there are cases where either a decrease or no change has also been observed. Three typical examples are shown in (a) $Pd_{40}Cu_{30}Ni_{10}P_{20}$ glass, (b) $Al_{89}La_6Ni_5$ glass, and (c) $Fe_{72}P_{11}C_6Al_5B_4Ga_2$ glass. (Reprinted from Jiang, J.Z. et al., *J. Appl. Phys.*, 87, 2664, 2000. With permission.)

The rate of nucleation, I can be represented by the equation

$$I = I_0 \exp\left(-\frac{\Delta G^* + \Delta G^d}{RT}\right)$$

where

I_0 is a constant

ΔG^* is the thermodynamic activation barrier, that is, free energy required to form the critical nucleus

ΔG^d is the activation energy for diffusion (to transport atoms across the interface)

R is the universal gas constant

T is the temperature

$\Delta G^* + \Delta G^d = \Delta G$ is the total energy required for the nucleation

$$\Delta G^* = \frac{16\pi\sigma^3}{3\Delta G_v^2} = \frac{16\pi\sigma^3}{3\left(G_c - G_a\right)^2}$$

where

σ is the interfacial energy between the amorphous and crystalline phases

G_c and G_a are the Gibbs free energies of the crystalline and amorphous phases, respectively

At a given temperature and pressure, ΔG^* can be expressed as

$$\left(\Delta G^*\right)_{P,T} = \frac{16\pi\sigma^3 \left(V_c\right)^2}{3\left[P\left(V_a - V_c\right) - \Delta G^{a\to c} + E\right]^2}$$

where

V_c and V_a are the molar volumes of the crystalline and amorphous phases, respectively $\Delta G^{a\to c} = G_c - G_a$

E is the elastic energy induced by the volume change when the phase transformed from the amorphous to the crystalline state

Assuming a negligible pressure dependence of $\Delta G^{a\to c}$, E, and σ, we can see that ΔG^* decreases with increasing pressure and therefore crystallization is favored.

$$\left(\frac{\partial G}{\partial P}\right)_T = -\frac{32\pi\sigma^3}{3\left(\Delta G^{a\to c}\right)^3}\left(V_c - V_a\right) + \left(\frac{\partial \Delta G^d}{\partial P}\right)_T$$

($V_c < V_a$; $-$ in the denominator; $-$ outside; $+$ on the second term; $+$ below)

Whether increasing pressure promotes or retards crystallization is determined by the magnitudes of the two terms.

Ex) polymorphous mode→no atomic redistribution → always promotes crystallization

Effect on high pressure torsion(HPT) process on BMGs

Structural rejuvenation

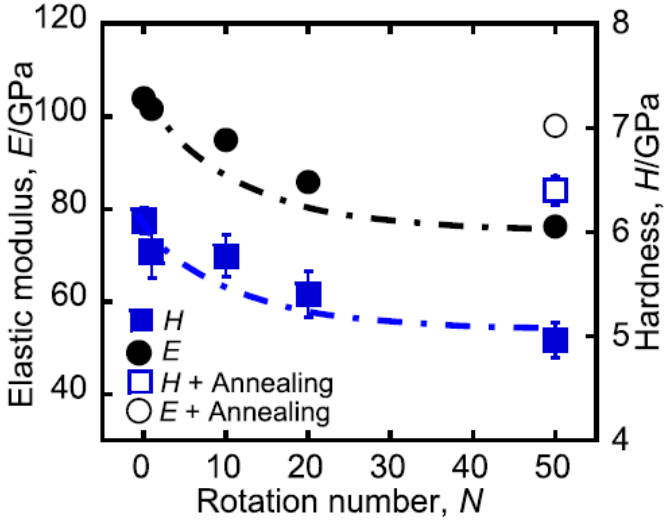

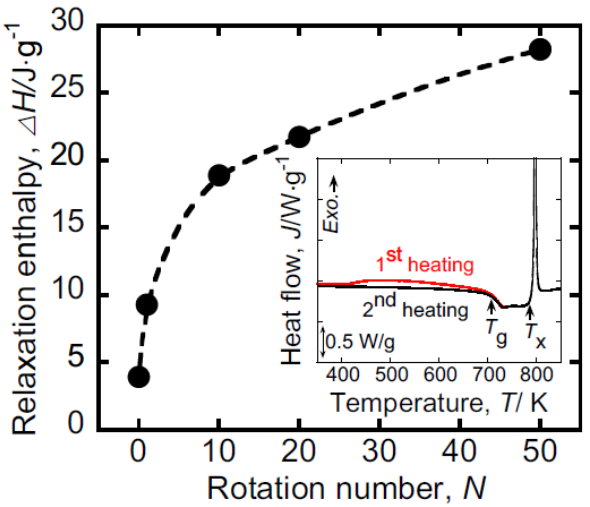

Mechanical softening

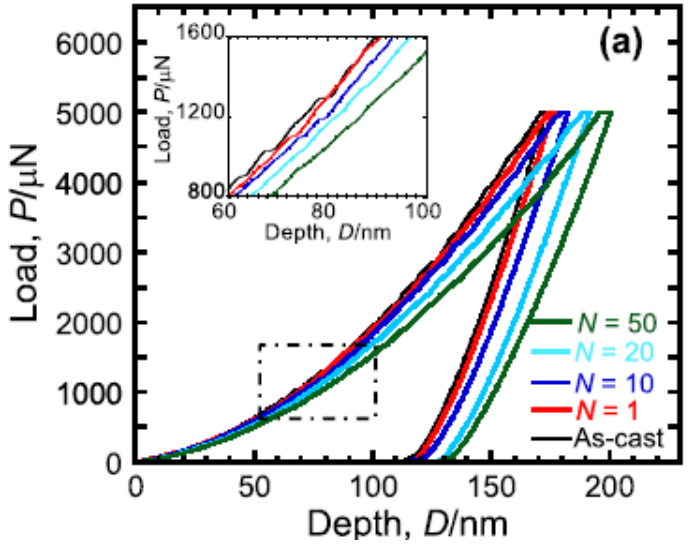

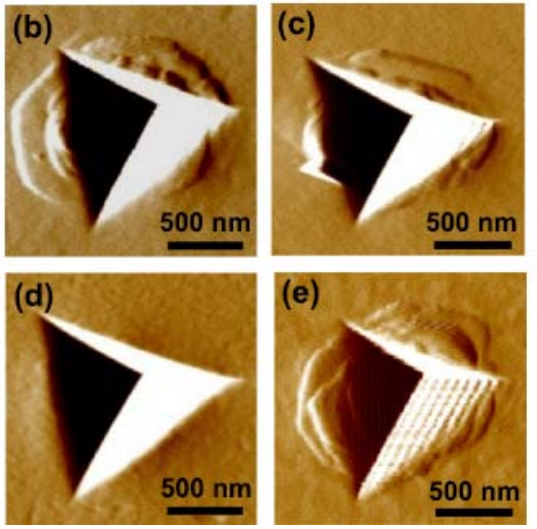

F. Meng et al (2012)

DSC analysis of Zr BMG/ZrN composites after HPT process

Zr BMGs

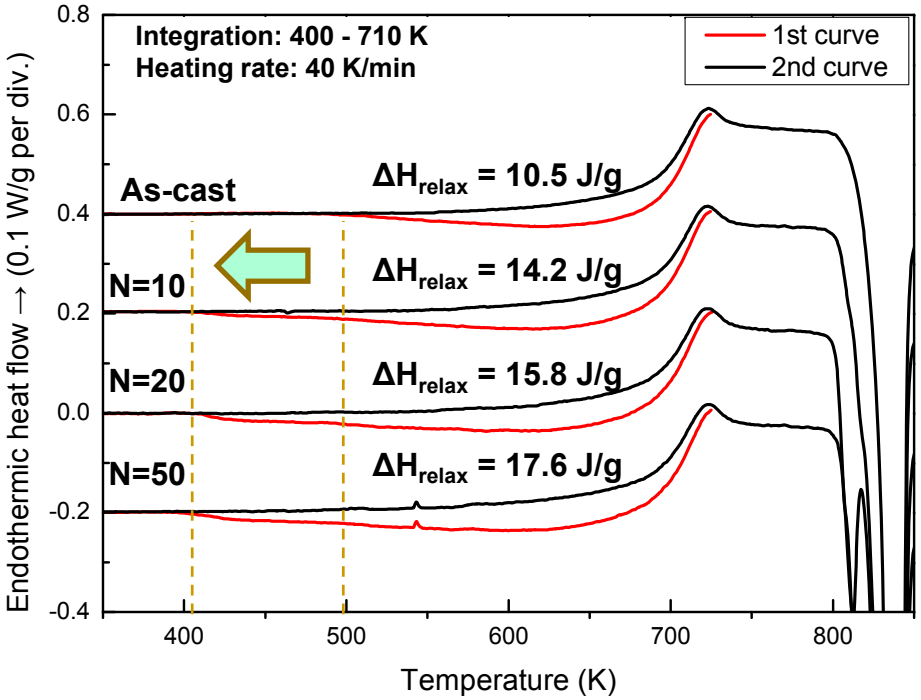

Zr BMG/ZrN composites

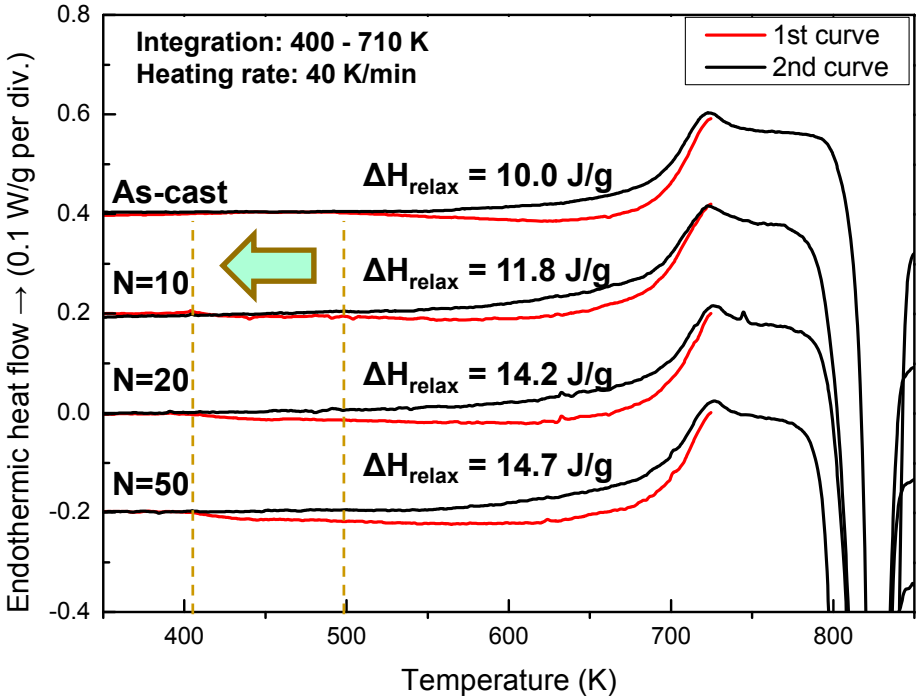

- **Enthalpy of relaxation was increased as # of rotation increased**
- **Enthalpy of relaxation for BMG composites was lower than that for monolithic BMGs.**
- **Relaxation onset temperature of the samples was reduced compared to as-cast sample.**

Structural relaxation of Zr BMG/ZrN composites after HPT process

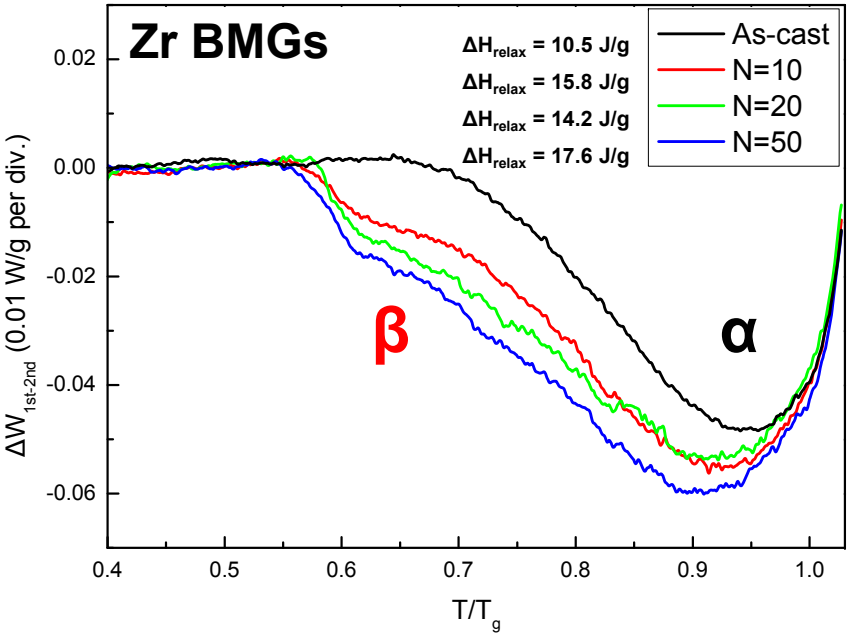

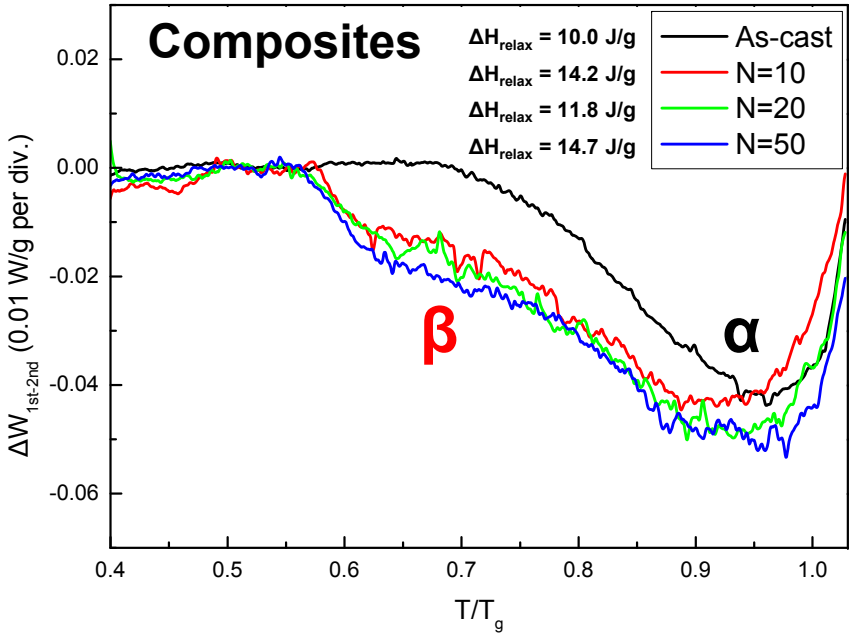

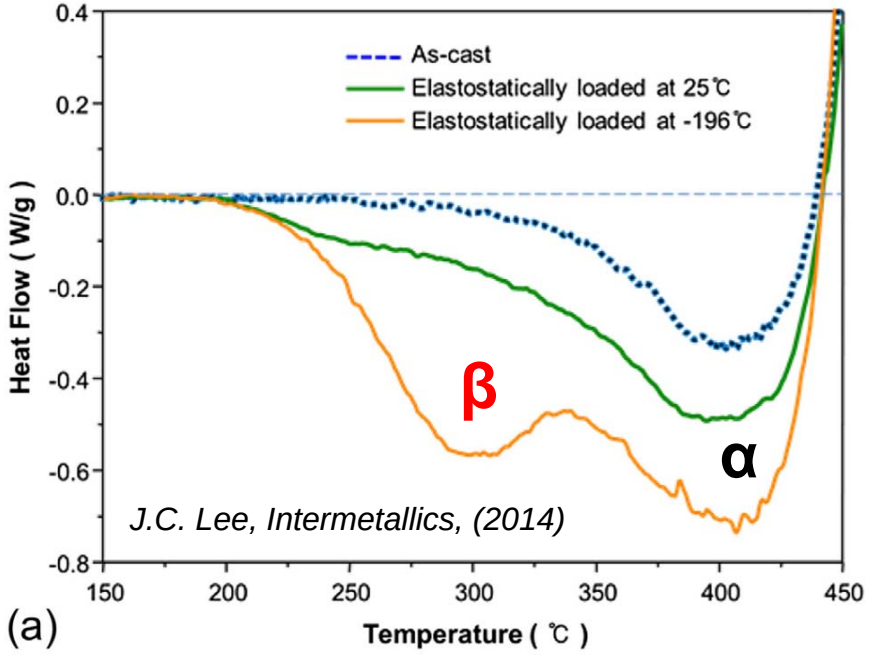

α relaxation
annihilation of short range order
(loose packing, free volume)

β relaxation
annihilation of medium range order
(shear transformation zones)

High pressure torsion of BMGs
→ Short, medium range structural disordering
→ Activation of β relaxation

Homework:

Summary (page 265 – page 360)

Chapter 6_Physical Properties & Chapter 7_Corrosion Behavior

You should submit your summary until 17 June. ☺